Chemical Science

ROYAL SOCIETY OF CHEMISTRY

EDGE ARTICLE

View Article Online
View Journal | View Issue

Cite this: *Chem. Sci.*, 2024, **15**, 5694

All publication charges for this article have been paid for by the Royal Society of Chemistry

Predicting valence tautomerism in diverse cobalt–dioxolene complexes: elucidation of the role of ligands and solvent†

F. Zahra M. Zahir, Moya A. Hay, Jett T. Janetzki, Robert W. Gable, Lars Goerigk * and Colette Boskovic *

The ability of molecular switches to reversibly interconvert between different forms promises potential applications at the scale of single molecules up to bulk materials. One type of molecular switch comprises cobalt–dioxolene compounds that exhibit thermally-induced valence tautomerism (VT) interconversions between low spin Co(III)-catecholate (LS-Co^{III}-cat) and high spin Co(II)-semiquinonate (HS-Co^{II}-sq) forms. Two families of these compounds have been investigated for decades but have generally been considered separately: neutral [Co(diox)(sq)(N_2L)] and cationic [Co(diox)(N_4L)]$^+$ complexes (diox = generic dioxolene, N_2L/N_4L = bidentate/tetradentate N-donor ancillary ligand). Computational identification of promising new candidate compounds prior to experimental exploration is beneficial for environmental and cost considerations but requires a thorough understanding of the underlying thermochemical parameters that influence the switching. Herein, we report a robust approach for the analysis of both cobalt–dioxolene families, which involved a quantitative density functional theory-based study benchmarked with reliable quasi-experimental references. The best-performing M06L-D4/def2-TZVPP level of theory has subsequently been verified by the synthesis and experimental investigation of three new complexes, two of which exhibit thermally-induced VT, while the third remains in the LS-Co^{III}-cat form across all temperatures, in agreement with prediction. Valence tautomerism in solution is markedly solvent-dependent, but the origin of this has not been definitively established. We have extended our computational approach to elucidate the correlation of VT transition temperature with solvent stabilisation energy and change in dipole moment. This new understanding may inform the development of VT compounds for applications in soft materials including films, gels, and polymers.

Received 27th August 2023
Accepted 8th March 2024

DOI: 10.1039/d3sc04493a

rsc.li/chemical-science

1 Introduction

The exploration of earth-abundant 3d transition metals for molecular materials is receiving increased attention, in part due to their access to different oxidation and spin-states. This oxidation and spin-state versatility allows for the synthesis of transition metal complexes that can switch between two or more discrete electronic states *via* an external stimulus such as heat, light or pressure. Such complexes may form the basis for materials with applications ranging from sensing and display devices to quantum information processing, spin filters and logic gates.[1–8] For some applications, switchable molecules need to be incorporated into soft materials such as polymer matrices, gels or liquid crystals, for example for flexible devices.[9–13] The development of these materials relies on the accessibility of specific properties suitable for the application; for example, a known transition temperature, solvent response or colour change. This requirement mandates a detailed understanding of the thermodynamic effects that control the molecular switching and resulting properties.

The phenomenon of spin crossover (SCO) is an example of spin switching between the low spin (LS) and high spin (HS) state in a transition metal compound.[14] Spin crossover has been explored for applications including thermal regulation, electrical conductance and actuation.[12,15–18] Spin crossover research has benefited greatly from unified computational approaches to analysing different families of SCO compounds.[19–21]

Complementary to SCO is the phenomenon of valence tautomerism (VT),[22] which involves a reversible intramolecular electron transfer between a redox-active metal and redox-active ligand.[23–25] Like SCO, VT is typically thermally induced; however, the requirement for redox activity at both the metal

School of Chemistry, University of Melbourne, Victoria 3010, Australia. E-mail: c.boskovic@unimelb.edu.au; lars.goerigk@unimelb.edu.au

† Electronic supplementary information (ESI) available: Details of computational, experimental, and synthetic methods, additional discussion, IR, TGA, powder X-ray diffraction, UV-vis and electrochemistry, crystallography, structural analysis, magnetic measurements, DFT (PDF). DFT optimized XYZ coordinates of monocationic complexes (ZIP). CCDC 2287380–2287385 (**15.BPh$_4$**), 2287386–2287395 (**19.BPh$_4$**) and 2287379 (**17.BPh$_4$.0.75DCM**) contain crystallographic data (CIF). CCDC 2287379–2287395. For ESI and crystallographic data in CIF or other electronic format see DOI: https://doi.org/10.1039/d3sc04493a

and ligand confers more extensive prerequisites to achieve VT than for SCO. The inherent redox activity required for VT offers additional possibilities for applications relating to redox chemistry or charge transfer. Moreover, insights into the complex interplay of ligand and metal interactions can have broader implications, including for metalloenzymes that utilise redox-activity,[26–28] conductive materials[29,30] and photochemical catalysis.[31]

Octahedral cobalt complexes with *ortho*-dioxolene (diox) ligands provide the majority of examples of VT.[32] Interconversion in these complexes generally occurs between low spin Co(III)-catecholate (LS-Co^{III}-cat) and high spin Co(II)-semiquinonate (HS-Co^{II}-sq) forms.[24,32–34] The HS-Co^{II}-sq form exhibits longer metal–ligand bond lengths and increased electronic degeneracy. Thus, a thermally-induced VT interconversion is observed upon heating the LS-Co^{III}-cat tautomer to afford the HS-Co^{II}-sq tautomer and is driven by the greater electronic and vibrational entropy of the HS-Co^{II}-sq form. The transition temperature ($T_{1/2}$) is defined as the temperature at which the LS-Co^{III}-cat and HS-Co^{II}-sq are in equal proportions;[23] it is the temperature at which the enthalpy and entropy terms of the corresponding Gibbs free energy equation are equal. Experimentally, the occurrence of a thermally-induced VT interconversion (and its $T_{1/2}$) for a Co–dioxolene complex depends on both the dioxolene and ancillary ligands.[24] In the solid state, crystal packing, intermolecular interactions and anions also affect the VT behaviour.[35–37] In solution VT interconversions are typically gradual,[35] with the $T_{1/2}$ significantly influenced by solvent.[38] The exact origin of this solvent dependency remains unclear, with specific solute–solvent interactions and solvent polarity and donor strength hypothesised to play a role.[38–41]

Despite numerous examples of Co–dioxolene VT complexes since the first report in 1980,[22] a generalised analysis of VT complexes has not been performed. Two major families of mononuclear Co–dioxolene complexes have been studied, generally in isolation from each other: the neutral [Co(diox)(sq)(N_2L)] and cationic [Co(diox)(N_4L)]$^+$ complexes (N_2L/N_4L = bidentate/tetradentate N-donor ancillary ligand) (Fig. 1). Even within the larger cationic [Co(diox)(N_4L)]$^+$ family, an analysis including the various types of N_4L ligand is yet to be reported. Given the parallel achievements in SCO research,[19–21] our primary goal at the outset of this study was to consolidate the diverse families of Co–dioxolene complexes together to: (i) gain a fundamental understanding of the underlying thermodynamic properties and be able to predict the occurrence of VT, and (ii) to elucidate the effect of solvent in tuning VT equilibrium and predict the solution $T_{1/2}$ values in different solvents.

Undoubtedly, the future of synthetic chemistry lies with *in silico* molecular design and screening techniques.[42] Computational approaches, such as density functional theory (DFT),[43,44] have emerged as a powerful tool to analyse chemical properties. Computation can be used to generate predictive models for the design and selection of molecular switches with a specific property. However, when applying DFT methods to study switchable metal complexes, issues arise when methods are chosen based on popularity without a proper benchmark

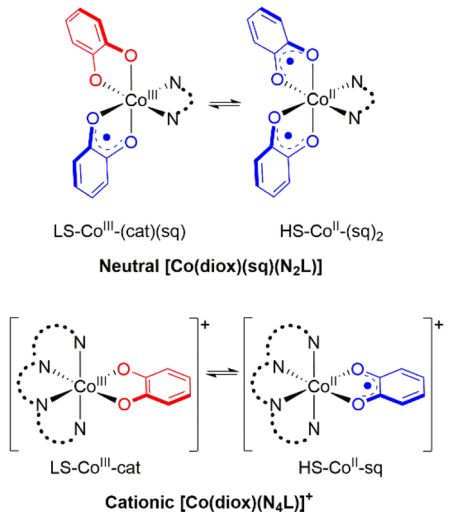

Fig. 1 Valence tautomeric interconversions for [Co(diox)(sq)(N_2L)] and [Co(diox)(N_4L)]$^+$ families of Co–dioxolene complexes.

study.[45,46] This can unknowingly lead to reliance on error cancellations and erroneous delocalisation of the electron density (delocalisation error), compromising the accuracy of predictions. Additionally, the common neglect of London dispersion effects by omission of dispersion corrections affects geometries, vibrational frequencies and electronic energies: see ref. 47–50 for reviews and examples. Valence tautomerism involves a change in oxidation/spin state and open shell configurations, complicating DFT-based modelling and resulting in a 'black box' treatment.[33,51–53] All these factors make computational analysis of VT complicated and any analysis of a broad range of VT complexes requires a careful choice of DFT method with rigorous benchmarking against experimental data.

Previously, some of us have shown it is possible to use benchmarked DFT methods to predict VT in a Co–dioxolene complex with subsequent experimental validation.[33] For VT to occur, the LS-Co^{III}-cat tautomer must be lower in energy than the HS-Co^{II}-sq tautomer, with a relatively small energy separation between them. We have also recently used benchmarked DFT methods to identify the M06L-D4/def2-TZVPP[54–56] method to rationalise and predict VT for neutral [Co(diox)(sq)(N_2L)] complexes.[42]

In the present work, we have made a significant extension to the use of *in silico* methods to understand the molecular origin of VT in Co–dioxolene complexes by unifying the cationic [Co(diox)(N_4L)]$^+$ and neutral [Co(diox)(sq)(N_2L)] families. This study is presented in four parts: (1) development of an accurate experimentally-benchmarked DFT-based strategy for predicting the tautomeric state of [Co(diox)(N_4L)]$^+$ complexes to verify that the method employed previously for [Co(diox)(sq)(N_2L)] is also applicable for [Co(diox)(N_4L)]$^+$; (2) unification of over forty [Co(diox)(N_4L)]$^+$ complexes for prediction and cross validation followed by an extensive analysis to understand the thermodynamic properties and establish a requisite energy region for VT

to occur; (3) prediction and experimental verification of two new VT $[Co(diox)(N_4L)]^+$ complexes and one temperature-invariant LS-Co^{III}-cat complex based on the calculated energy regions; and (4) understanding the role of solvent in the VT equilibrium for both $[Co(diox)(N_4L)]^+$ and $[Co(diox)(sq)(N_2L)]$ families. The developed understanding will facilitate future efforts to design VT complexes with molecular features tailored for specific applications.

2 Methods

2.1 Computational details

All calculations for this study were performed using ORCA[57–59] versions 4.0–5.0. All other computational settings and further details are described in ESI Section 1: Computational details.†

2.1.1 Geometry optimisation. For the geometry optimisation of 45 monocationic complexes, the computationally inexpensive BP86 (ref. 60–62) functional and triple-ζ def2-TZVP atomic orbital basis set[56] with Grimme's DFT-D3 dispersion correction with Becke–Johnson damping (D3(BJ))[47,48] were employed in the gas phase. Geometries for the five neutral complexes were obtained from ref. 42 that had been optimised with hybrid PBEh-3c[63] that includes a double-ζ basis set, dispersion correction and correction for basis-set superposition errors (see ESI Section 1: Computational details†)

2.1.2 Quasi-experimental reference. Establishment of the initial benchmark utilised complexes **1–6**, (Chart 1). Solvent effects were determined for complexes **1–6**, employing the conductor-like polarisable continuum model (CPCM)[64,65] using BP86-D3(BJ)/def2-TZVP. Calculations were performed using acetonitrile (MeCN) for complexes **1–4**; with dichloromethane (DCM) for complex **5**; and DCM, MeCN and 1,2-dichloroethane (DCE) for complex **6**. Both LS-Co^{III}-cat and HS-Co^{II}-sq tautomeric forms were calculated as single point energies in the gas phase. The total energies of both tautomers were obtained with CPCM and their energy differences (with and without the solvent model) were calculated to obtain the relative solvent correction/solvent stabilisation energy (ΔE_S).

Scalar relativistic effects were estimated using the zeroth order regular approximation (ZORA)[66] using BP86-D3(BJ) with the ZORA-def2-TZVP[59] basis set. Both LS-Co^{III}-cat and HS-Co^{II}-sq tautomeric forms were calculated as single point energies in the gas phase. Then, both tautomeric energies were obtained with the ZORA relativistic model employed. The energy difference between the two systems (with and without relativistic effects) were calculated to obtain the relativistic correction (ΔE_R).

Thermal vibrations were calculated after the geometry optimisation with a frequency analysis using BP86-D3(BJ)/def2-TZVP at relevant temperatures. Thermal corrections (ΔE_T) were calculated to account for the thermal vibrational effects and zero-point energies, at either the experimental temperatures for non-VT complexes or the transition temperatures for the VT complexes (for details on the different corrections and how they were calculated, see ESI Section 1: Computational details†).

2.1.3 Density functional benchmarking for valence tautomer energies. Our quasi-experimental, gas phase reference values serve as a benchmark. The related DFT benchmark study involved single point calculations that were performed for the model complexes with the fully polarised def2-TZVPP[56] basis set in the gas phase with 21 different functionals paired with various dispersion corrections: DFT-D3(BJ), DFT-D3(0), the VV10 non-local kernel,[67] and DFT-D4,[55,68] with the last two accounting for charge and multiplicity (Table 1). The deviation/error of the functional from the quasi-experimental values were individually calculated for all six complexes and averaged for each methodology to obtain both mean signed error (MSE) and mean absolute error (MAE).

2.1.4 Calculations of solvent effects. Exploration of the effect of solvent in Section 4 employed the optimised geometries. The respective thermal corrections (from PBEh-3c) for the selected neutral complexes were obtained from ref. 42. Geometries and thermal corrections for monocationic complexes were obtained with BP86-D3(BJ)/def2-TZVP. All other corrections (solvent and relativistic) were re-determined and standardised with M06L-D4/def2-TZVPP for the selected neutral and monocationic complexes.

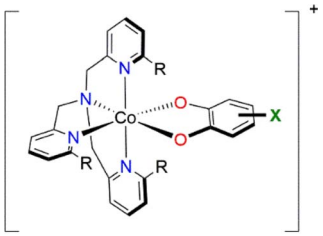

1: $[Co(3,5\text{-dbdiox})(tpa)]^+$
2: $[Co(3,5\text{-dbdiox})(Metpa)]^+$
3: $[Co(3,5\text{-dbdiox})(Me_2tpa)]^+$
4: $[Co(3,5\text{-dbdiox})(Me_3tpa)]^+$
5: $[Co(Cl_4diox)(Me_3tpa)]^+$
6: $[Co(Br_4diox)(Me_3tpa)]^+$

Chart 1 Initial set of reference $[Co(Xdiox)(Me_ntpa)]^+$ complexes (tpa = tris(2-pyridylmethyl)amine with methylation, X = 3,5-di-*tert*-butyl, Cl_4, Br_4) used in this work with numbering scheme. R = H or Me for Me_ntpa; n = 0–3.

2.2 Synthesis

Compounds of predicted complexes $[Co(H_4diox)(Me_2tpa)].BPh_4$ (**15.BPh$_4$**), $[Co(4\text{-tbdiox})(tpa)].BPh_4$ (**17.BPh$_4$**) and $[Co(4\text{-tbdiox})(Me_2tpa)].BPh_4$ (**19.BPh$_4$**) were obtained by first coordinating the tpa or Me_2tpa ancillary ligand to the divalent cobalt metal centre, followed by addition of deprotonated catechol or 4-*tert*-butylcatechol (under N_2 atmosphere). The material obtained was then oxidised with ferrocenium tetraphenylborate and sonicated[69] affording pure compounds with 80–90% yield. The compounds were characterised by solution and solid-state magnetic measurements electrochemistry, crystallography, electronic absorption spectroscopy and other measurements. Further details are described in ESI Section 2: Experimental and synthetic procedures.†

Table 1 DFT methods used for this study

Functional type	Method[a,b]
GGA	BP86-D3(BJ)[47,60–62] OPBE[70,71] OPBE-D3(BJ)[70–72] OPBE-D4 [55,70,71] B97M-V[73] B97-3c[74] B97M-D3(BJ)[73,75]
Meta-GGA	M06L-D3(0)[54,72] M06L-D4 [54,55]
Global hybrids	B3LYP-D3(BJ)[47,76,77] B3LYP-D4 [55,76,77] TPSSh-D3(BJ)[72,78] TPSSh-D4 [55,78]
Range-separated hybrids	ωB97X-V[79] ωB97M-V[80] ωB97M-D3(BJ)[75,80] ωB97X-D3(BJ)[75,79]
Global double hybrids	B2PLYP-D3(BJ)[72,81] B2PLYP-D4 [55,81] PWPB95-D3(BJ)[72,82] PWPB95-D4 [55,82]

[a] The citations include the functional and the article that has published its dispersion-correction parameters. [b] def2-TZVPP was used for each method except for B97-3c, which has its own basis set def2-mTZVP. D3(0): DFT-D3 with zero-damping;[48] D3(BJ): DFT-D3 with Becke–Johnson damping; D4: DFT-D4 [55,68] V: VV10 van-der-Waals DFT kernel.[67]

3 Results and discussion

3.1 DFT benchmark study

Determination of the most reliable DFT method for analysing any given family of VT complexes is achieved by benchmarking against experimentally investigated complexes. In principle, the energy difference between the two tautomeric forms ($\Delta E = E_{\text{HS-Co(II)-sq}} - E_{\text{LS-Co(III)-cat}}$) can be used to identify the likelihood of valence tautomerism. Establishing an appropriate threshold for this interconversion would be an ideal diagnostic criterion. In general, VT in mononuclear Co–dioxolene complexes occurs through a one-step process between LS-Co$^{\text{III}}$-cat and HS-Co$^{\text{II}}$-sq, although on rare occasions VT has been observed as a charge transfer with no accompanying spin transition.[83,84] For simplicity, the LS-Co$^{\text{II}}$-sq state is not considered in this study.

To explore whether the computational model previously determined as most reliable for the neutral [Co(diox)(sq)(N_2L)] complexes[42] is also suitable for the cationic [Co(diox)(N_4L)]$^+$, we first independently considered the cationic family. We have previously determined that the M06L-D4/def2-TZVPP method performs extremely well for [Co(3,5-dbdiox)(3,5-dbsq)(N_2L)] (N_2L = diimine, 3-5dbsq = 3,5-di-*tert*-butylsemiquinonate) in a benchmark study.[42] Thus, we approached our goal by first examining the large family of cationic [Co(Xdiox)(N_4L)]$^+$ (Xdiox = derivatised dioxolene) complexes with various types of tetradentate N-donor ancillary ligands.[33,35,69,85–89]

Valence tautomerism in [Co(Xdiox)(N_4L)]$^+$ complexes is highly sensitive to even small changes in N_4L ligand substitution. This sensitivity was exploited in the [Co(3,5-dbdiox)(Me$_n$tpa)]$^+$ family by varying methyl substitution on the Me$_n$tpa ancillary ligand; thermally-induced VT was observed only for $n = 2$, while $n = 0$, 1 and $n = 3$ stabilised the LS-Co$^{\text{III}}$-cat and HS-Co$^{\text{II}}$-sq state, respectively.[85] The highly sensitive nature of the charge distribution of these complexes is also evident in prior DFT studies;[33,90] a calculated truncated model of [Co(3,5-dbdiox)(Me$_2$tpa)]$^+$ to give [Co(H_4diox)(Me$_2$tpa)]$^+$ was found to have a HS-Co$^{\text{II}}$-sq ground state in one study[90] whilst a LS-Co$^{\text{III}}$-cat ground state in another,[33] highlighting the absolute need to develop accurate computational protocols for this system. Hence, this section aims to identify a properly tested robust computational approach by benchmarking against experimentally reported thermochemical values. For VT in Co–dioxolene complexes, experimentally observed thermodynamic parameters in solution generally lie within the ranges ΔH = 20–60 kJ mol^{-1} and ΔS = 80–150 J K^{-1} mol^{-1}.[33,86,91]

3.1.1 Model complexes. The first step in the benchmark of the cationic Co–dioxolene complexes was the selection of six Me$_n$tpa based complexes of general formula [Co(Xdiox)(Me$_n$-tpa)]$^+$ (X = 3,5-di-*tert*-butyl, Cl_4 and Br_4; n = 0–3) shown in Chart 1 (complexes **1–6**), which have reported experimental thermochemical parameters (Table 2). These complexes were chosen as they span the three possible charge distributions: **1** and **2** remain as LS-Co$^{\text{III}}$-cat, **4** remains as HS-Co$^{\text{II}}$-sq, and **3**, **5** and **6** display thermally induced VT interconversion.[33,85,86] For [Co(Xdiox)(Me$_n$tpa)]$^+$ complexes, the tautomeric state is tuned *via* two methods: the steric requirements of the Me$_n$tpa ancillary ligand modulate the Co redox potential and orbital energies, while the electronic properties of the Xdiox ligand tune the dioxolene redox potentials and orbital energies. The less sterically crowded the Me$_n$tpa (with fewer methyl groups), and the more electron withdrawing the Xdiox substituents, the greater the stabilisation of LS-Co$^{\text{III}}$-cat.

3.1.2 Quasi-experimental energies. Optimised geometries were obtained for the selected model complexes **1–6** (Fig. S1–S6†). We then individually quantified the most prominent modulating effects before "back-correcting" these effects from the experimental data to acquire "quasi-experimental" data.[92] For each complex, solvent (ΔE_S), relativistic (ΔE_R), and thermal effects (ΔE_T), were individually quantified and subtracted from experimental enthalpy changes (ΔH) to obtain quasi-experimental energies (ΔQ_E) as shown in eqn (1) (Table 2). More details are provided in ESI Section 3: DFT results, and Tables S1–S6†.

$$\Delta Q_E = \Delta H - (\Delta E_S + \Delta E_R + \Delta E_T) \quad (1)$$

The quantified effects and the obtained ΔQ_E values are shown in Table 2. It is worth noting how the combined impact of the three various corrections are significant, with the largest difference between ΔQ_E and ΔH being 40.8 kJ mol^{-1} for complex **1**. This resulted in the calculated data for the six reference complexes to correspond to isolated gas phase molecules at 0 K (without vibrational or relativistic effects), rendering a benchmark that is easily compared to various Co–dioxolene molecules in the gas phase. This acts as an interface between the condensed phase systems and various chemical environments enabling comparison among various computational methods (see ESI Section 3: DFT results for details†).

Table 2 The six $[Co(Xdiox)(Me_ntpa)]^+$ model complexes, the experimentally observed valence tautomer, respective solvent, transition temperature ($T_{1/2}$), and the experimental enthalpy changes (ΔH) for each complex, the individually quantified corrections for solvent (ΔE_S), relativistic (ΔE_R) and thermal effects (ΔE_T) calculated with BP86-D3(BJ)/def2-TZVP and the resulting quasi-experimental energies (ΔQ_E)

		Experimental			Calcd. correction/kJ mol^{-1}			
Model complex	Reported valence tautomer	Solvent ($T_{1/2}$/K)	ΔH^a/kJ mol^{-1}	Ref.	ΔE_S	ΔE_R	ΔE_T	ΔQ_E/kJ mol^{-1}
1	LS-Co^{III}-cat	MeCN	61	85	32.7	11.8	−3.7	20.2
2	LS-Co^{III}-cat	MeCN	34	85	32.8	11.1	−5.4	−4.5
3	VT	MeCN^b	6	85	29.5	10.8	−3.5	−30.8
4	HS-Co^{II}-sq	MeCN	−25	85	29.9	9.8	−3.0	−61.7
5	VT	DCM/250	31	86	32.3	10.2	−5.7	−5.8
6	VT	DCM (291)	35	33	32.7	9.4	−5.3	−5.7^c
		DCE (295)	32	33	33.3	9.4	−5.2	
		MeCN (359)	32	33	37.1	9.4	−4.6	

^{a} Experimental ΔH for complexes **1–4** in ref. 85 were derived from Gibbs free energy changes acquired through voltametric measurements in MeCN at 298 K, with an added component of entropy changes estimated from Fe-analogues. For complex **5**, ΔH was determined using electronic absorption spectroscopy in DCM and for complex **6**, Evans NMR method was employed in DCM, DCE and MeCN. ^{b} $T_{1/2}$ not reported. ^{c} Average of ΔQ_E of three experimental conditions are used for complex **6**.

3.1.3 Density functional screening for valence tautomer energies. Next, we performed a density functional screening of a total of 21 dispersion-corrected and uncorrected functionals to identify a suitable functional for the valence tautomer energies. (See ESI discussion 3: DFT results, Fig. S7, S8, Tables S7 and S8†). The functional M06L-D4 worked very well in this benchmark study, which also performed very well in our recent benchmark study of neutral $[Co(3,5\text{-dbdiox})(3,5\text{-dbsq})(N_2L)]$.[42] Hence, we selected M06L-D4/def2-TZVPP for the calculation and prediction of cationic Co–dioxolene complexes. This unified approach enables for the first time, the direct comparison of neutral and cationic Co–dioxolene families of complexes.

3.2 Establishing a target energy range for valence tautomerism

Having identified M06L-D4/def2-TZVPP as a suitable level of theory for both monocationic and neutral Co–dioxolene complexes, we sought to extend the method to the entire cationic $[Co(Xdiox)(N_4L)]^+$ family of complexes. We searched the Cambridge Structural Database (CSD) to identify, to the best of our knowledge, all structurally characterised monocationic Co–dioxolene complexes with N_4L ancillary ligands (Chart 2). We found data for thirty-two cobalt complexes with N_4L ancillary ligands (derivatives of Me_ntpa, quinoline,[87] azamacrocycle,[69] cyclam,[37,89,93] pyrazole[94] and other amine derivatives[88]) paired with a range of dioxolene ligands incorporating electron donating, electron withdrawing and aromatic substituents.

Using this large set of molecules, we proceeded to study the valence tautomer energies of the complexes to understand the underlying thermodynamic effects and trends to establish a target energy range for which VT is likely to occur. To assess the accuracy of the results, we also included an additional thirteen hypothetical $[Co(Xdiox)(Me_ntpa)]^+$ complexes ($X = Cl_4$ ($n = 1, 2$), Br_4 ($n = 0, 1, 2$), H_4 ($n = 0$–3), 4-tb ($n = 0$–3)). These systems were chosen to further study the effect of slight structural modifications and the steric effect of the N_4L ancillary *vs.* electronic effect of the Xdiox. From these thirteen complexes (**8–20**), predictions could be made for the most likely complex to display VT, which can be experimentally validated to confirm the accuracy of our DFT protocol (Table 3).

We have therefore calculated the gas-phase spin-state energetics of the monocationic Co–dioxolene complexes **1–45** (Fig. 2) using M06L-D4/def2-TZVPP at 0 K excluding any thermal, relativistic or solvent effects (Table 3). The calculated relative spin-state energies for the thirty-two reported complexes (**1–7**, **21–45**) and thirteen hypothetical complexes (**8–20**) were then included in an energy diagram (Fig. 2), affording three energy regions corresponding to the three possible charge distributions: LS-Co^{III}-cat region (blue), HS-Co^{II}-sq region (red) and a potential VT region (green). Complex **36** ($[Co(3,5\text{-dbdiox})(Et_2AzaN)]^+$) for which the onset of VT occurs at 333 K in DCE, and complex **23** ($[Co(Andiox)(Me_2tpa)]^+$) with the smallest relative electronic energy observed of the VT complexes,[96] form the respective upper and lower limits of the VT region. The prospective VT energy region lies between −20 and −4 kJ mol^{-1} for monocationic Co–dioxolene complexes calculated at the M06L-D4/def2-TZVPP level in the gas phase. Complexes with an energy separation above the VT upper limit (>−4 kJ mol^{-1}) will remain as the LS-Co^{III}-cat form regardless of temperature, and those below (<−20 kJ mol^{-1}) remain in the HS-Co^{II}-sq state. Complexes with energies in between/close to this VT limit are thus potential VT candidates. The established energy regions enabled us to assign the calculated tautomeric states to the respective relative spin-state energies (ΔE_{Gas}) for complexes **1–45**.

Overall, the tautomeric forms of all reported molecules, except complex **39** are accurately captured in the calculations. For **39**, the calculated energy appears to favour a VT transition and it was found to exist in the HS-Co^{II}-sq state under applied pressure. However, without a crystal structure the spatial arrangement, and the nature of **39** is not precisely known. Therefore, the accuracy of the calculations to reflect experimental observations is over 97%, illustrating the robust and quantitative nature of the applied DFT method.

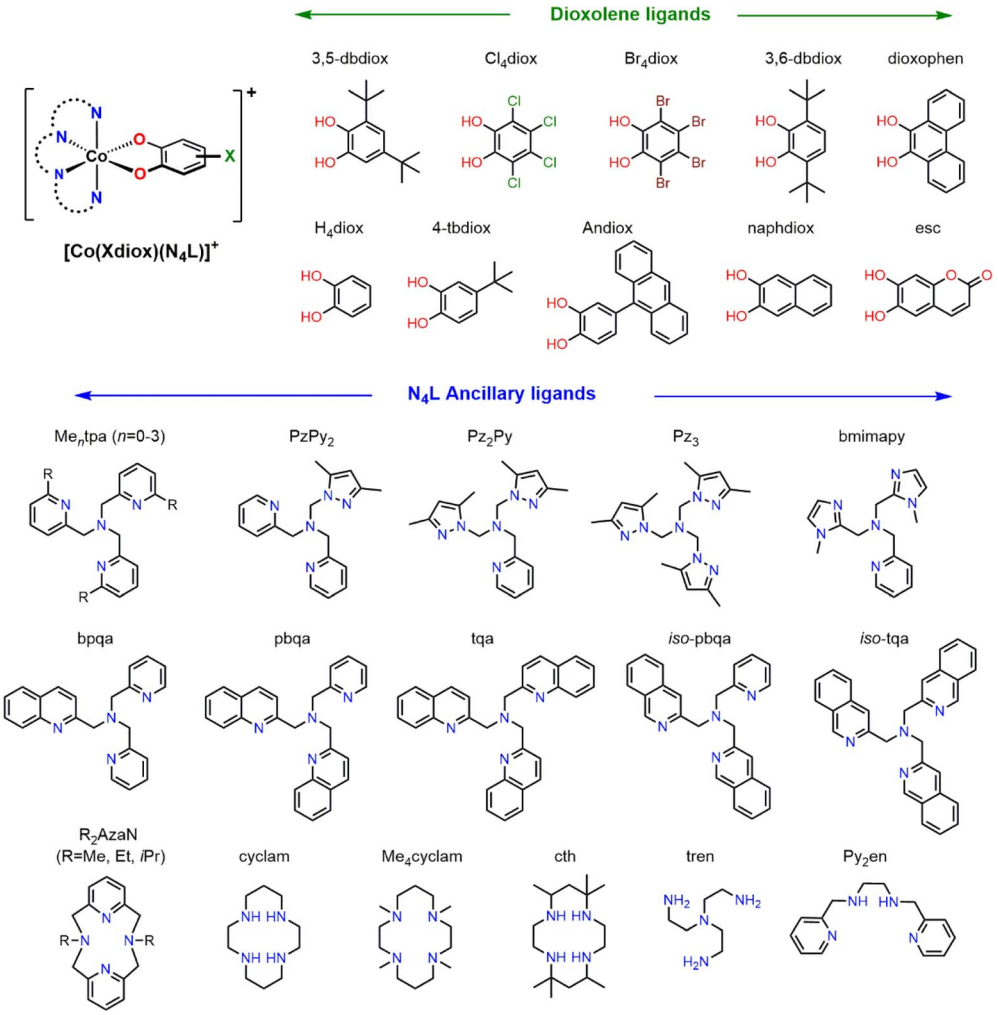

Chart 2 $[Co(Xdiox)(N_4L)]^+$ complexes with varying dioxolene and ancillary ligands.

Our DFT based approach has also allowed quantification of the steric effects imposed by the N_4L ancillary ligands and the significant influence on the charge distribution of mono-cationic Co–dioxolene complexes. (ESI Section 4: Effect of redox-active *vs.* ancillary ligand, Table S12†).

The precision of the three energy regions will enable researchers to identify whether a hypothetical molecule can exhibit VT or is likely to remain in a temperature-invariant LS-Co^{III}-cat or HS-Co^{II}-sq form. For the hypothetical complexes **8–20**, we predict that only $[Co(H_4diox)(Me_2tpa)]^+$ (**15**) and [Co(4-tbdiox)$(Me_2tpa)]^+$ (**19**) should show VT, with **8–14**, **17**, **18** remaining as LS-Co^{III}-cat and **16** and **20** remaining as HS-Co^{II}-sq. Two previous computational studies suggested complex **15** would remain as HS-Co^{II}-sq (TPSSh/6-311++G(d,p))[90] or LS-Co^{III}-cat (OPBE/ZORA/TZP/CPCM).[33] Therefore, on top of the 97% success rate for reported $[Co(Xdiox)(N_4L)]^+$ complexes, we aimed to validate the accuracy of our established energy regions experimentally for predicted VT complexes **15** and **19**, as well as the anticipated LS-Co^{III}-cat complex **17**.

3.3 Experimental validation

Complexes **15**, **17** and **19** were synthesised as tetraphenylborate salts in good yield and characterised using various techniques to examine the charge distribution and possibility of thermally-induced VT to validate the calculated VT energy range.

3.3.1 Structure description. Solid-state structures of compounds of **15**, **17** and **19** were determined by single crystal X-ray diffraction studies (Fig. 3).

Compound **15.BPh$_4$** crystallises in the space group *Pna*2_1, with two crystallographically unique cobalt complexes and two BPh_4^- anions in the asymmetric unit without solvent. Compound **19.BPh$_4$** crystallises in the $P2_1/n$ space group with one cobalt complex and one BPh_4^- anion in the asymmetric unit without solvent. Compound **17.BPh$_4$**·0.75 DCM crystallises in the $P2_1$ space group with two unique cobalt complexes, two BPh_4^- anions and 1.5 DCM molecules in the asymmetric unit. The octahedral cobalt complexes **15**, **19** and **17** all exhibit bidentate coordination of the respective dioxolene ligands and tetradentate coordination of the ancillary ligands (Fig. 3, ESI Section 4: structural data and description and Tables S13–S15†).

Table 3 $[Co(Xdiox)(N_4L)]^+$ complexes selected for this study from the literature, the reported valence tautomer, ΔE_{Gas} calculated in this work using M06L-D4/def2-TZVPP and calculated valence tautomer

Complex[a]		Reported valence tautomer[b]	Ref.	Calcd. ΔE_{Gas}[c]/kJ mol^{-1}	Calcd. valence tautomer[d]
$[Co(3,5\text{-dbdiox})(tpa)]^+$	**1**	LS-Co^{III}-cat	85	16.1	LS-Co^{III}-cat
$[Co(3,5\text{-dbdiox})(Metpa)]^+$	**2**	LS-Co^{III}-cat	85	−0.8	LS-Co^{III}-cat
$[Co(3,5\text{-dbdiox})(Me_2tpa)]^+$	**3**	VT	85	−17.1	VT
$[Co(3,5\text{-dbdiox})(Me_3tpa)]^+$	**4**	HS-Co^{II}-sq	85	−38.0	HS-Co^{II}-sq
$[Co(Cl_4diox)(Me_3tpa)]^+$	**5**	VT	86	−11.7	VT
$[Co(Br_4diox)(Me_3tpa)]^+$	**6**	VT	33	−12.7	VT
$[Co(Cl_4diox)(tpa)]^+$	**7**	LS-Co^{III}-cat	95	32.3	LS-Co^{III}-cat
$[Co(Cl_4diox)(Metpa)]^+$	**8**	—	—	16.6	LS-Co^{III}-cat
$[Co(Cl_4diox)(Me_2tpa)]^+$	**9**	—	—	2.1	LS-Co^{III}-cat
$[Co(Br_4diox)(tpa)]^+$	**10**	—	—	35.7	LS-Co^{III}-cat
$[Co(Br_4diox)(Metpa)]^+$	**11**	—	—	22.3	LS-Co^{III}-cat
$[Co(Br_4diox)(Me_2tpa)]^+$	**12**	—	—	5.1	LS-Co^{III}-cat
$[Co(H_4diox)(tpa)]^+$	**13**	—	—	22.1	LS-Co^{III}-cat
$[Co(H_4diox)(Metpa)]^+$	**14**	—	—	11.8	LS-Co^{III}-cat
$[Co(H_4diox)(Me_2tpa)]^+$	**15**	—	—	−8.9	VT
$[Co(H_4diox)(Me_3tpa)]^+$	**16**	—	—	−30.6	HS-Co^{II}-sq
$[Co(4\text{-tbdiox})(tpa)]^+$	**17**	—	—	14.1	LS-Co^{III}-cat
$[Co(4\text{-tbdiox})(Metpa)]^+$	**18**	—	—	3.6	LS-Co^{III}-cat
$[Co(4\text{-tbdiox})(Me_2tpa)]^+$	**19**	—	—	−17.2	VT
$[Co(4\text{-tbdiox})(Me_3tpa)]^+$	**20**	—	—	−38.3	HS-Co^{II}-sq
$[Co(Andiox)(tpa)]^+$	**21**	LS-Co^{III}-cat	96	16.3	LS-Co^{III}-cat
$[Co(Andiox)(Metpa)]^+$	**22**	VT	96	−7.7	VT
$[Co(Andiox)(Me_2tpa)]^+$	**23**	VT	96	−19.1	VT
$[Co(Andiox)(Me_3tpa)]^+$	**24**	HS-Co^{II}-sq	96	−33.9	HS-Co^{II}-sq
$[Co(3,6\text{-dbdiox})(Me_2tpa)]^+$	**25**	VT	97	−9.9	VT
$[Co(3,5\text{-dbdiox})(bpqa)]^+$	**26**	LS-Co^{III}-cat	87	−1.8	LS-Co^{III}-cat
$[Co(3,5\text{-dbdiox})(pbqa)]^+$	**27**	VT	87	−13.5	VT
$[Co(3,5\text{-dbdiox})(tqa)]^+$	**28**	HS-Co^{II}-sq	87	−39.1	HS-Co^{II}-sq
$[Co(3,5\text{-dbdiox})(\textit{iso}\text{-pbqa})]^+$	**29**	LS-Co^{III}-cat	98	21.1	LS-Co^{III}-cat
$[Co(3,5\text{-dbdiox})(\textit{iso}\text{-tqa})]^+$	**30**	LS-Co^{III}-cat	98	22.8	LS-Co^{III}-cat
$[Co(dioxophen)(cyclam)]^+$	**31**	LS-Co^{III}-cat	37	0.3	LS-Co^{III}-cat
$[Co(dioxophen)(cth)]^+$	**32**	VT[e]	37	−18.0	VT
$[Co(dioxophen)(Me_4cyclam)]^+$	**33**	HS-Co^{II}-sq	37	−49.4	HS-Co^{II}-sq
$[Co(3,5\text{-dbdiox})(Me_2AzaN)]^+$	**34**	LS-Co^{III}-cat	99	−3.1	LS-Co^{III}-cat
$[Co(3,5\text{-dbdiox})(\textit{i}Pr_2AzaN)]^+$	**35**	VT	69	−4.7	VT
$[Co(3,5\text{-dbdiox})(Et_2AzaN)]^+$	**36**	VT	69	−4.2	VT
$[Co(Br_4diox)(tren)]^+$	**37**	LS-Co^{III}-cat	100	8.3	LS-Co^{III}-cat
$[Co(3,5\text{-dbdiox})(PzPy_2)]^+$	**38**	LS-Co^{III}-cat	94	4.6	LS-Co^{III}-cat
$[Co(3,5\text{-dbdiox})(Pz_2Py)]^+$	**39**	HS-Co^{II}-sq[e]	94	−16.5	VT
$[Co(3,5\text{-dbdiox})(Pz_3)]^+$	**40**	HS-Co^{II}-sq	94	−29.4	HS-Co^{II}-sq
$[Co(3,5\text{-dbdiox})(bmimapy)]^+$	**41**	VT	101	−4.7	VT
$[Co(Cl_4diox)(bmimapy)]^+$	**42**	LS-Co^{III}-cat	101	9.3	LS-Co^{III}-cat
$[Co(esc)(Py_2en)]^+$	**43**	LS-Co^{III}-cat	102	17.1	LS-Co^{III}-cat
$[Co(Cl_4diox)(Py_2en)]^+$	**44**	LS-Co^{III}-cat	95	24.4	LS-Co^{III}-cat
$[Co(naphdiox)(tpa)]^+$	**45**	LS-Co^{III}-cat	103	30.8	LS-Co^{III}-cat

[a] The structures of relevant ancillary and dioxolene ligands are shown in Chart 2 with abbreviations indicated in Table S10. [b] Complexes **1–7**, **21–45** are reported, and complexes **8–20** are hypothetical. [c] The absolute energies of the tautomers are provided in Table S11. [d] The calculated valence tautomers are determined based on the energy regions established in Fig. 2. [e] Measurements in the solid state.

The metric parameters (Table 4) from the structural analysis of the three compounds provide important information about the oxidation and spin state of the cobalt ions and dioxolene ligands. The oxidation state of cobalt can be determined by examining the Co–O and Co–N (N_1–$N_3 = N_{py}$, $N_4 = N_{amine}$) bond lengths and the selected octahedral distortion parameters (Σ, Θ and octahedral SHAPE).[104–106] In general, the LS-Co^{III}-cat form exhibits shorter Co–O/N bond lengths (∼1.8 Å) with minimal distortion while the Co–O/N bond lengths can increase by 0.18–0.21 Å for HS-Co^{II}-sq tautomer (∼2.1 Å), with a higher degree of distortion in the octahedral environment. The oxidation states of the coordinated dioxolene ligand can be assigned by the empirical metrical oxidation state (MOS), using a least-squared fitting of C–C and C–O bond distances of dioxolene ligands to assign an apparent oxidation state: −2 for a catecholate oxidation state and −1 for a semiquinonate oxidation state.[107]

At 100 K, **15.BPh$_4$**, **19.BPh$_4$** and **17.BPh$_4$**·0.75 DCM all exhibit small SHAPE indices and octahedral distortion parameters (Σ

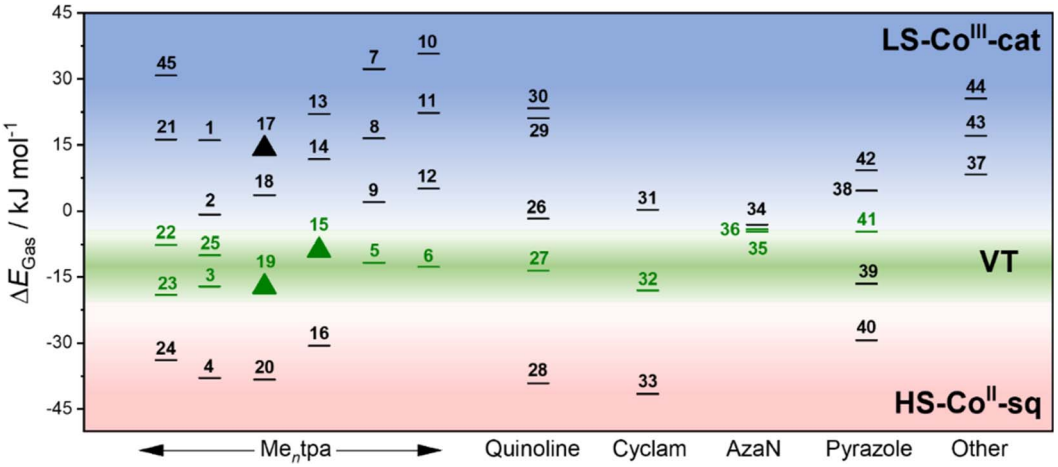

Fig. 2 Energy diagram representing the calculated energy separations between the valence tautomers of the reported (**1–7**, **21–45**) and hypothetical (**8–20**) [Co(Xdiox)(N_4L)]$^+$ complexes. Black lines represent either temperature invariant LS-Co^{III}-cat or HS-Co^{II}-sq states. Green lines represent experimentally confirmed complexes that display thermally induced VT. Green triangles (▲) indicate the predicted VT complexes and black triangle (▲) indicate the predicted LS-Co^{III}-cat complex chosen for experimental verification in this study.

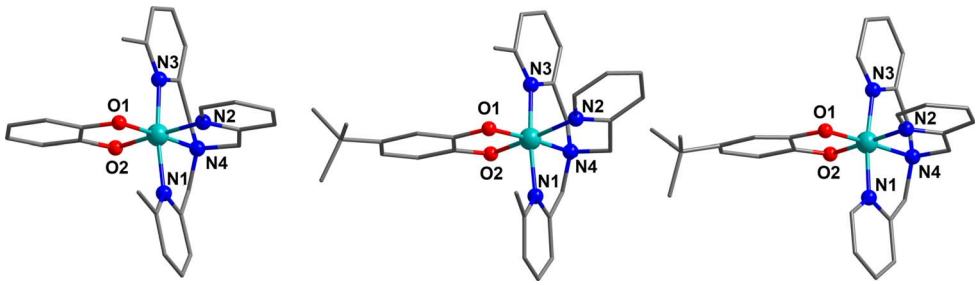

Fig. 3 Molecular structures of **15** in **15**.BPh$_4$ (left), **19** in **19**.BPh$_4$ (middle) and **17** in **17**.BPh$_4$·0.75 DCM (right). Colour code: carbon, grey; oxygen, red; nitrogen, blue: cobalt, aqua green, (hydrogen atoms omitted for clarity).

and Θ), consistent with minimal distortion from an ideal octahedron (Table 4 and Fig. S9†).[36,37] The coordination sphere of each molecule at 100 K displays shorter Co–O/N bond lengths, with a calculated MOS closer to −2, indicative of a LS-Co^{III}-cat form.[24] Upon increasing the temperature, both **15.BPh$_4$** and **19.BPh$_4$** undergo significant increases in Co–O/N bond lengths coupled with the MOS approaching −1 (Table 4 and Fig. 4).

The increase in SHAPE, Σ and Θ parameters for the two compounds upon heating is suggestive of distortion, inherent to a HS-Co^{II}-(sq) form (Fig. S9 and S10†). Therefore, **15.BPh$_4$** and **19.BPh$_4$** appear to undergo thermally-induced VT in the solid-state, with the latter being more complete (Fig. 4). For **17.BPh$_4$**·0.75 DCM, measurements were obtained only at 100 K due to rapid degradation of the crystals. Although a direct comparison between single-complex calculations and solid-state measurements is not always advisable, the average Co–O and Co–N bond lengths determined for **15** and **19** from DFT-based optimised structures (BP86-D3(BJ)/def2-TZVP) of both LS-Co^{III}-cat and HS-Co^{II}-sq states are in agreement with the experimental values (Fig. S10†) illustrating the charge distribution.

Powder X-ray diffraction (PXRD) diffractograms of crystalline bulk samples of all three complexes matched well with the calculated patterns (Fig. S11†) indicating phase purity. The bulk recrystallised compounds are consistent with the formulae **15.BPh$_4$**, **19.BPh$_4$** and **17.BPh$_4$** (with no DCM molecules) for the complexes with analytical purity and absence of solvent confirmed by elemental analysis and thermogravimetric analysis. The charge distribution of the complex in solid-state is also verified by infra-red spectroscopy (ESI Sections 6, 7, Fig. S12, S13 and Table S16†).

3.3.2 Solid-state magnetic measurements. To confirm the charge distribution in the solid-state, solid-state magnetic susceptibility measurements were performed on bulk crystalline samples of **15.BPh$_4$**, **19.BPh$_4$** and **17.BPh$_4$** (Fig. 4). The magnetic measurements are presented as the product of molar magnetic susceptibility multiplied by temperature ($\chi_M T$) *vs.* temperature. Compound **17.BPh$_4$** is diamagnetic with a $\chi_M T$ value of ∼0.02 cm^3 K mol^{-1} across the entire temperature region (2–400 K), confirming a LS-Co^{III}-cat tautomeric form. Compounds **15.BPh$_4$** and **19.BPh$_4$** both display an increase in $\chi_M T$ upon increasing temperature, matching the observed crystallographic data, confirming VT behaviour (Fig. 4). Upon increasing the temperature from 2 to 400 K, the $\chi_M T$ of **15.BPh$_4$** and **19.BPh$_4$** increases from 0.17 to 1.62 cm^3 K mol^{-1} and 0.11 to 3.13 cm^3 K mol^{-1}, respectively, indicating an incomplete VT transition for **15.BPh$_4$** and a complete VT transition for

Table 4 Selected interatomic distances (Å), octahedral distortion and oxidation state parameters for compounds **15**.BPh_4, **19**.BPh_4 and **17**.BPh_4·ϖ0.75 DCM

	15.BPh_4				**19**.BPh_4		**17**.BPh_4·0.75 DCM	
Parameter	100 K (A)[a]	100 K (B)[a]	370 K (A)[a]	370 K (B)[a]	100 K	400 K	100 K (A)[a]	100 K (B)[a]
Intramolecular bond lengths/Å								
Co–O_1	1.860(3)	1.885(3)	1.881(5)	1.897(5)	1.856(16)	1.996(17)	1.873(4)	1.866(4)
Co–O_2	1.883(3)	1.863(4)	1.908(6)	1.876(5)	1.903(16)	2.133(18)	1.890(5)	1.875(4)
Co–N_1	2.013(4)	1.979(4)	2.039(7)	2.006(6)	2.015(19)	2.173(18)	1.917(6)	1.949(5)
Co–N_2	1.925(4)	1.954(4)	1.948(5)	1.977(5)	1.976(17)	2.138(18)	1.911(5)	1.921(5)
Co–N_3	2.016(4)	2.034(4)	2.075(5)	2.026(6)	1.978(17)	2.167(17)	1.975(6)	1.934(5)
Co–N_4	1.949(4)	1.946(4)	1.982(5)	1.976(4)	1.948(16)	2.119(16)	1.917(6)	1.905(4)
Distortion and oxidation state parameters								
SHAPE (Oh)[b]	0.289	0.340	0.494	0.491	0.446	1.400	0.180	0.175
Σ/°[c]	37.8	43.5	52.6	60.0	55.3	99.9	34.2	31.2
Θ/°[d]	100.6	108.4	135.8	137.7	126.0	250.1	90.8	87.3
MOS[e]	−1.9(2)	−2.1(2)	−1.6(2)	−1.7(3)	−1.9(2)	−1.1(1)	−1.8(2)	−1.8(2)

[a] A and B for **15**.BPh_4 and **17**.BPh_4·0.75 DCM represent the two crystallographic independent molecules. [b] SHAPE index for octahedral geometry calculated in SHAPE 2.1 (ref. 104 and 105). [c] $\sum = \sum_{i=1}^{12} |90 - \alpha_i|$ where α_i are the twelve *cis*–O/N–Co–O/N angles about the cobalt atom. [d] $\Theta = \sum_{j=1}^{24} |60 - \Theta_j|$ where Θ_j are the 24 unique O/N–C_a–C_b–O/N dihedral angles, $|\Theta_j| < 120°$, measured on the centroids of the two triangular faces of the octahedron along their common *pseudo*-threefold axis. Σ and Θ were calculated in OctaDist – a program used to determine the structural distortion of the octahedral complexes.[106] [e] Metrical oxidation state as described in the text.

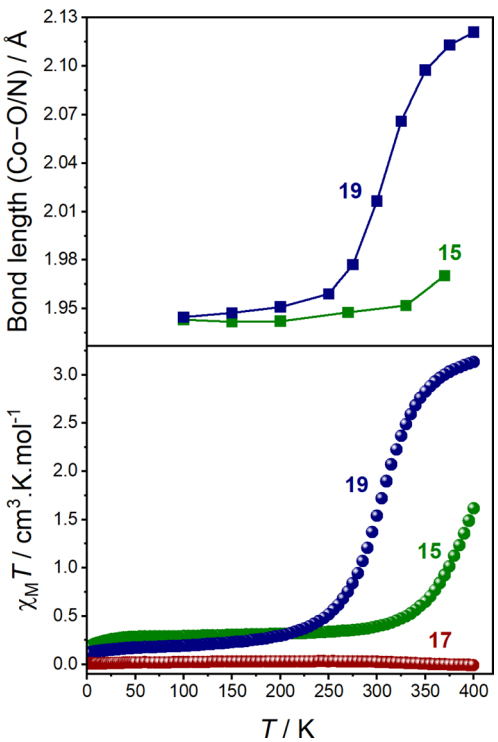

Fig. 4 (Top) change in average Co–O/N bond length *vs.* *T* for **15**.BPh_4 (green squares) and **19**.BPh_4 (blue squares); and (bottom) plot of $\chi_M T$ *vs.* *T* for the first heating of **15**.BPh_4 (green spheres), **19**.BPh_4 (blue spheres) and **17**.BPh_4 (red spheres).

19.BPh_4.[85,87] The reversibility of the transition for both complexes was established with multiple heating and cooling cycles Fig. S14.†

The solid-state magnetic and single crystal X-ray diffraction measurements thus verify the computational predictions that **15** and **19** undergo valence tautomerism while **17** remains as temperature invariant LS-Co^{III}-cat. The calculated tautomeric energy seperation of **15** (−8.9 kJ mol^{-1}) indicates greater stabilisation of the LS-Co^{III}-cat state compared to that of **19** (−17.2 kJ mol^{-1}), which is perfectly reflected in the solid-state magnetic data; **15** displays an incomplete VT transition, while **19** undergoes a complete VT transition. However, as solid-state behaviour is affected by crystal packing effects, we turned to solution measurements to further probe the VT transitions.

3.3.3 Electronic absorption spectroscopy. Room temperature electronic absorption spectra for complexes **15**, **17** and **19** measured in MeCN, butyronitrile (BuCN), acetone, DCE and DCM are available in Fig. S15 and Table S17† with relevant band assignments and discussions (see ESI Section 8: Electronic absorption spectroscopy†). The spectra of complex **17** indicate the LS-Co^{III}-cat state in all five solvents, while for **19** the spectra indicate the HS-Co^{II}-sq state in all solvents. For **15**, the spectra in MeCN, BuCN and acetone suggest the LS-Co^{III}-cat charge distribution, while in DCM and DCE the spectra are consistent with HS-Co^{II}-sq. Similar solvent dependency, specifically chlorinated solvents stabilising HS-Co^{II}-sq and nitrile solvents stabilising LS-Co^{III}-cat, has been reported in the literature for other complexes.[33,69]

Variable-temperature spectra of **15** and **19** were recorded to probe the VT behaviour in MeCN, BuCN, acetone, DCE and DCM (after verifying the solution stabilities, Fig. S16–S18†). Distinct and reversible changes in the spectra were evident for both **15** and **19** in all five solvents (Fig. 5, S20 and S21†). For **15**, in all five solvents, heating from 268 K resulted in the increased intensity of a band at ∼590 nm, consistent with increasing

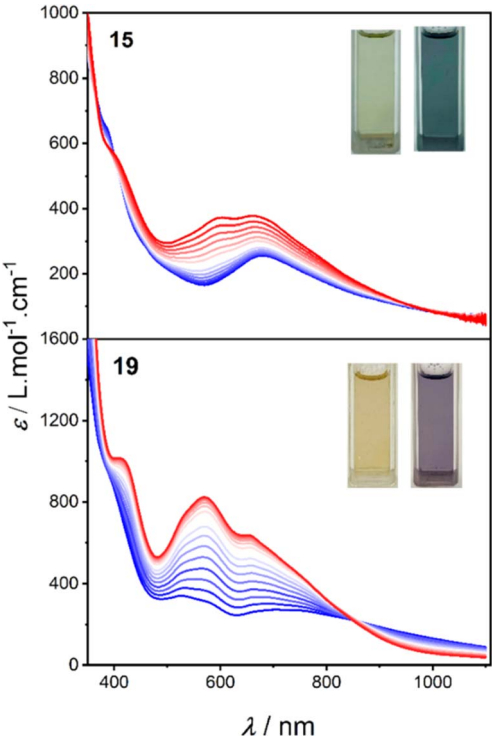

Fig. 5 Variable temperature electronic absorption spectra in MeCN for complexes **15** (273–333 K) and **19** (268–343 K). Figure insets are photographs of the low and high temperature solutions.

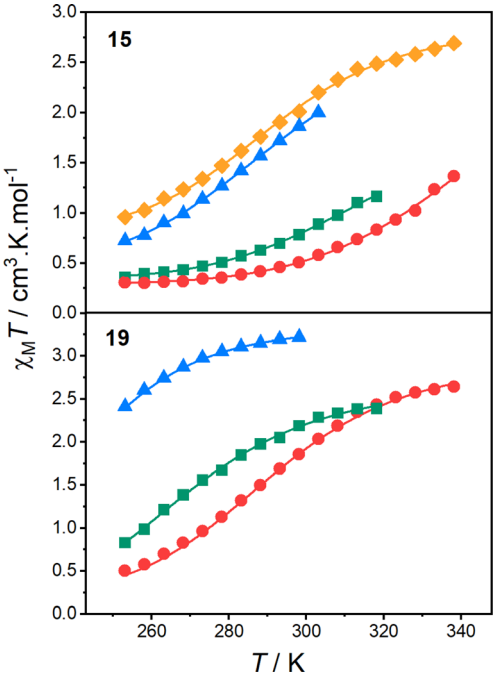

Fig. 6 Plots of $\chi_M T$ *vs.* T obtained *via* Evans NMR method for solutions of **15** (top) and **19** (bottom) in DCE (orange ◆), DCM (blue ▲), acetone (green ■) and MeCN (red ●). Respective solid lines indicate fits to the regular solution model.

formation of HS-Co^{II}-sq tautomer. For **19**, in MeCN, BuCN, and acetone, the same behaviour is observed. However, in DCM and DCE, minimal change is evident upon heating from 268 to 298 (DCM) or 319 K (DCE), suggesting that **19** is stabilised in the HS-Co^{II}-sq state around room temperature. Several isosbestic/near isosbestic points between ~400–950 nm are indicative of two interconverting species for **15** and **19**. The charge distribution of all three complexes was further verified from voltametric measurements (see ESI discussion in Section 9: Electrochemistry, Fig. S22, Tables S18 and S19†).

The electronic spectra of **17** confirms a LS-Co^{III}-cat state in solution (Fig. S19†), as well as the observation of VT for **15** and **19** in solution across various solvents. Importantly, they also demonstrate that the LS-Co^{III}-cat state is stabilised to a greater extent for **15** than for **19**, reflective of the solid-state magnetic behaviour and further validating the quantitative predictions of the DFT methodology. Complexes **15** and **19** exhibit different VT behaviour depending on the solvent and solution magnetic measurements were performed to determine the $T_{1/2}$ values in different solvents.

3.3.4 Solution magnetic measurements. Variable temperature solution magnetic susceptibility measurements were performed using the Evans NMR method for complexes **15**, **17** and **19** (ESI Section 10: Solution magnetic measurements, Fig. S23–S25 and Table S20†).[108,109] The data were recorded in deuterated MeCN, DCM, DCE and acetone (Fig. 6). The temperature range of measurement for each solvent was selected to be above the freezing point, so data were not measured for **19** in DCE as freezing obscures the transition. For **15** and **19**, a gradual increase is evident in $\chi_M T$ with increasing temperature across the solvents. The VT behaviour varies with the solvent, consistent with the electronic absorption spectra. At room temperature, **17** displaying $\chi_M T$ values of ~0.3 cm^3 K mol^{-1} in all solvents indicative of a LS-Co^{III}-cat charge distribution, with the variation of temperature causing no change.

Fitting the $\chi_M T$ *vs.* temperature data for **15** and **19** to the regular solution model (Fig. 6) afforded the thermodynamic parameters $T_{1/2}$, ΔH and ΔS (Table 5). Each model provided good fits ($R^2 > 0.99$) and afforded appropriate values. The ΔH varies minimally between 30–45 kJ mol^{-1} across the solvents, while ΔS varied to a greater degree between 90–160 J K^{-1} mol^{-1}, consistent with the previous analogues.[33,91,110]

The $T_{1/2}$ values for **15** are higher than for **19** in each solvent. This is consistent with the electronic absorption spectra and the solid-state magnetic data (Fig. 4). Therefore, the position of the two complexes in the energy diagram (Fig. 2), with **15** closer to the LS-Co^{III}-cat region and **19** closer to the HS-Co^{II}-sq region, is consistent with the behaviour observed in both the solid and solution-state and demonstrates the accuracy of the boundaries of the energy regions. It is clear therefore, that our DFT methodology can not only predict potential VT complexes, but also predict whether the transition occurs at a higher or lower temperature.

From the solution measurements, we have identified that the VT interconversions of **15** and **19** are solvent-tunable, with the increase in $T_{1/2}$ following the order: DCM < DCE < acetone < MeCN. This is consistent with literature observations for related complexes.[33,69] However, as mentioned above, the origin of this

Table 5 Thermodynamic parameters obtained for **15** and **19** by fitting the solution magnetic susceptibility data to the regular solution model

Complex	Solvent	ΔH/kJ mol^{-1}	ΔS/J mol^{-1} K^{-1}	$T_{1/2}$/K
15	DCE	39 ± 5	133 ± 11	293 ± 4
	DCM	37 ± 8	129 ± 14	286 ± 5
	Acetone	35 ± 4	106 ± 12	330 ± 4
	MeCN	40 ± 4	119 ± 9	344 ± 4
19	DCM	39 ± 8	160 ± 15	242 ± 5
	Acetone	39 ± 6	143 ± 12	273 ± 5
	MeCN	43 ± 4	149 ± 8	290 ± 4
	BuCN[a]	42 ± 9	161 ± 20	261 ± 7

[a] Thermodynamic parameter for BuCN is extracted from VT UV-vis measurements as indicate in Fig. S27 and S28.

solvent-dependence is unknown. Thus, as the final part of this work, we sought to utilise our quantitative DFT treatment to explore the effect of solvent on the VT equilibrium.

3.4 Solvent effects

Understanding the influence of solvent on the VT equilibrium will not only provide fundamental insights into VT, but will inform understanding of the effects of environment and therefore the future integration of VT components into materials for applications. To our knowledge, computational studies to explicitly investigate the effect of solvent on the VT equilibrium have not been performed previously. Thus, we sought to apply our established quantitative M06L-D4/def2-TZVPP strategy to both the neutral and cationic complexes with the aim of elucidating the origins of the solvent influence on VT for Co–dioxolene compounds in general.

Various explanations and correlations of different solvatochromic parameters have been proposed, including generic solvent properties and specific solvent–complex interactions like hydrogen or halogen bonding.[38,111,112] In general, for transition metal complexes that exhibit solvent tuning of the charge transfer energy, the effects postulated to play a role include change in dipole moment, reorganisation energy, and the energy separation between two states.[38,39,111,113] As observed for **15** and **19** (Fig. 6 and S15†) and several literature $[Co(Xdiox)(N_4L)]^+$ complexes, chlorinated and brominated solvents tend to stabilise the HS-Co^{II}-sq state, whereas nitrile solvents stabilise the LS-Co^{III}-cat form.[33,69] It has been hypothesised that the high donor number from MeCN stabilises the smaller metal centre in the LS-Co^{III}-cat form.[86] In other cases, the solvent polarity appears to play a larger role than the donor number, with the $T_{1/2}$ decreasing with increasing static dielectric constant (ε_r) and refractive index.[38] It has been observed for neutral [Co(3,5-dbdiox)(3,5-dbsq)(bpy)] that the switching temperatures in various solvents does not correlate with the dielectric constant.[93]

For this study, the three reference VT complexes (**3**, **5** and **6**), the newly reported VT complexes (**15** and **19**) and complexes **27**, **32**, **35** and **41** were selected to encompass the broad range of ancillary and dioxolene ligands in the $[Co(Xdiox)(N_4L)]^+$ VT family. We also chose neutral [Co(3,5-dbdiox)(3,5-dbsq)(N_2L)] (N_2L = 1,10′-phenanthroline (**46^0**); 1,2-bipyridine (**47^0**)) from our previous study.[42] Using these eleven complexes, we quantified the influence of the individual thermodynamical effects on VT by calculating contributions from thermal vibrations, relativistic and solvent effects. We employed acetonitrile in the calculations, owing to the generally observed solubility and stability of both neutral and monocationic complexes (Table 6 and Fig. 7). While ion-pairing effects and specific solute–solvent interactions can have some influence, they are complicated and their exploration is beyond the scope of this study.

In Fig. 7, the green region defines the range of values for total energy change (20–60 kJ mol^{-1}) that corresponds to an experimentally observed thermally-induced VT region. Experimental enthalpies result from multiple factors common for all VT complexes. By deconvoluting individual effects that contribute to the total energies, the different factors that affect the overall thermodynamic behaviour of the systems can be visualised. In

Table 6 The individual effects calculated as corrections, relative electronic energies, VT enthalpies in MeCN, and the change in dipole moment ($\Delta\mu$) of the complexes in MeCN

	Calculated correction/kJ mol^{-1}					
Complex	ΔE_S (MeCN)[a]	ΔE_R[a]	ΔE_T[b]	ΔE_{Gas}/kJ mol^{-1}	$\Delta H_{(calc)}$ (MeCN)[c]/kJ mol^{-1}	$\Delta\mu$ (MeCN)[d]/Debye
3	30.0	10.8	−3.5	−17.1	20.2	−6.71
5	34.7	9.6	−5.7	−11.7	26.9	−6.28
6	36.5	8.9	−4.6	−12.7	28.1	−6.20
15	30.6	10.6	−4.3	−8.9	28.0	−6.30
19	30.5	10.7	−3.6	−17.2	20.4	−6.90
27	31.9	11.1	−3.4	−13.5	26.1	−6.17
32	41.0	10.3	−3.4	−18.0	29.9	−7.04
35	24.8	9.7	−5.8	−4.7	24.0	−4.61
41	33.3	11.7	−5.4	−4.7	34.9	−6.16
46^0	8.3	13.0	−5.3	15.8	31.8	−2.87
47^0	8.4	13.3	−4.4	21.7	39.0	−2.82

[a] ΔE_R and ΔE_S obtained in gas phase as single point energies with M06L-D4/def2-TZVPP. [b] For neutral Co–dioxolenes, ΔE_T obtained *via* PBEh-3c optimised geometries while for monocationic Co–dioxolenes ΔE_T obtained *via* BP86-D3(BJ)/def2-TZVP optimised geometries. [c] $\Delta H_{(calc)}$ represents the calculated enthalpy changes that includes solvent (MeCN), relativistic and thermal corrections. [d] $\Delta\mu$ indicates ($\mu_{HS\text{-}CoII\text{-}sq} - \mu_{LS\text{-}CoIII\text{-}cat}$).

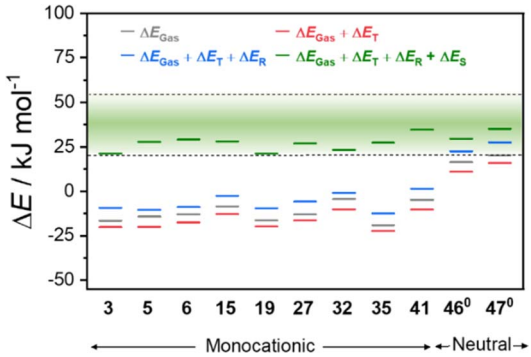

Fig. 7 Relative spin-state energy of VT monocationic $[Co(Xdiox)(N_4\text{-}L)]^+$ and neutral $[Co(3,5\text{-}dbdiox)(3,5\text{-}dbsq)(N_2L)]$ families illustrating the cumulative effects from the gas phase (ΔE_{Gas}) (grey); relative gas phase energy with thermal effects ($\Delta E_{Gas} + \Delta E_T$) (red); relative gas phase energy with thermal and relativistic effects ($\Delta E_{Gas} + \Delta E_T + \Delta E_R$) (blue); relative gas phase energy with thermal, relativistic and solvent effects in MeCN ($\Delta E_{Gas} + \Delta E_T + \Delta E_R + \Delta E_S$) (green). (The green region illustrates the experimental VT energy region in solution).

Fig. 7 and Table 6, the individual effects for thermal vibrations (ΔE_T), relativistic (ΔE_R) and solvent stabilisation (ΔE_S) are presented. First, the relative gas phase energy (ΔE_{Gas}) for the neutral complexes **46⁰** and **47⁰** is greater than the ΔE_{Gas} for all the monocationic complexes, indicating that the intrinsic relative energies of these two families of complexes are distinct due to the charge and the variation in coordination environment. The changes in relativistic (average ΔE_R of 10.4 and 13.1 kJ mol^{-1} for the neutral and cationic complexes, respectively) and thermal (average ΔE_T of −4.4 and −4.9 kJ mol^{-1} for the neutral and cationic complexes, respectively) effects are similar for the two families. However, stabilisation effects from the solvent (ΔE_S) differ significantly: an average of 8.4 and 32.6 kJ mol^{-1} for the neutral and cationic complexes, respectively. It is worth noting that, beside ΔE_{Gas}, the quantified ΔE_R, ΔE_T and ΔE_S do not drastically vary with the functional (ESI Section 3: DFT results, Tables S4–S6†), proving the validity of the calculated quantities for the two families. Combination of the calculated gas phase energies, with the corresponding solvent stabilisation energies in MeCN, brought all the complexes into the illustrative experimental VT region (Fig. 7).

By consolidating the neutral and cationic complexes, we have demonstrated that underlying VT energetics for the monocationic *versus* neutral complexes differ. In particular the solvent stabilisation energies are much larger and more significant for the cationic complexes *versus* the neutral. With this understanding, we sought to elucidate the effect of solvent on VT $T_{1/2}$ using a case-by-case analysis and correlation with experimental observations.

3.4.1 Case 1: effect of various solvents on a single complex. To determine the impact of various solvents on the $T_{1/2}$ value of a specific complex, we used the two newly synthesised VT complexes **15** and **19**. The number of solvents examined was constrained by the solubility and stability of the complexes. We therefore investigated the effects of MeCN, BuCN, DCM, DCE and acetone had on ΔE_S. The calculated ΔE_S values were then associated with the respective experimental $T_{1/2}$ values for **15** and **19** in the different solvents (Table 7 and Fig. 8).

For both **15** and **19**, an excellent correlation of calculated ΔE_S with the experimentally measured $T_{1/2}$ values ($R^2 > 0.98$) is observed, demonstrating a larger ΔE_S (*i.e.*, larger stabilisation of LS-Co^{III}-cat by the solvent) correlates with higher $T_{1/2}$ value.

Table 7 Calculated ΔE_S, $\Delta E_S + \Delta E_{Gas}$ and experimentally measured $T_{1/2}$ for complex **15** and **19** in various solvents

Complex	Solvent	ΔE_S[a]/kJ mol^{-1}	$\Delta E_S + \Delta E_{Gas}$[a]/kJ mol^{-1}	$T_{1/2}$/K
15	MeCN	30.6	21.7	344
	Acetone	29.7	20.8	330
	DCM	27.1	18.2	286
	DCE	27.7	18.8	293
19	MeCN	30.5	13.3	290
	Acetone	29.6	12.4	273
	DCM	27.0	9.8	242
	DCE	27.6	10.4	—

[a] ΔE_S and $\Delta E_S + \Delta E_{Gas}$ are calculated with M06L-D4/def2-TZVPP as $E_{HS\text{-}CoII\text{-}sq} - E_{LS\text{-}CoIII\text{-}cat}$.

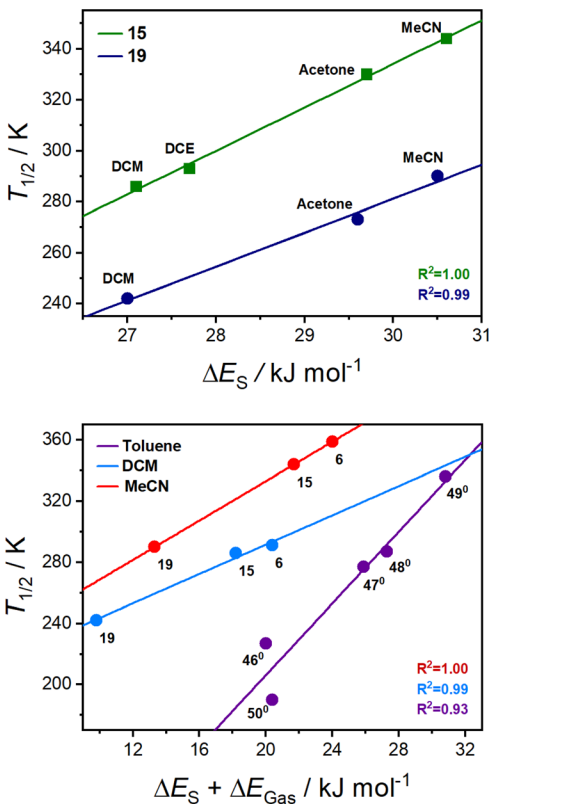

Fig. 8 (Top) correlation of the experimentally determined $T_{1/2}$ values with respective calculated ΔE_S for complex **15** (green $R^2 = 1.00$; $T_{1/2} = 17.0 \times \Delta E_S - 178$) and complex **19** (blue $R^2 = 0.99$; $T_{1/2} = 13.3 \times \Delta E_S - 118$) in various solvents. (Bottom) correlation of the experimentally determined $T_{1/2}$ values with calculated $\Delta E_S + \Delta E_{Gas}$ for complexes (**15**, **19** and **6**) in MeCN solution (red; $R^2 = 1.00$, $T_{1/2} = 6.4 \times \{\Delta E_S + \Delta E_{Gas}\} + 204$) and DCM solution (blue; $R^2 = 0.99$, $T_{1/2} = 4.8 \times \{\Delta E_S + \Delta E_{Gas}\} + 195$) and neutral (**46⁰–50⁰**) complexes considered in Chart S1† in toluene solution (purple; $R^2 = 0.90$, $T_{1/2} = 11.7 \times \{\Delta E_S + \Delta E_{Gas}\} - 29$).

Hence, MeCN with a larger ΔE_S compared to DCM, will result in higher $T_{1/2}$ values. Similar solvent trends have been reported from experimental investigations of complexes **6** (ESI Section 11: Correlations and thermodynamic parameters, Table S21 and Fig. S26†) and **35**.[33,69] The established correlation between the calculated solvent parameters and experimental $T_{1/2}$ provides a tool for predicting the $T_{1/2}$ in a specific solvent.

To demonstrate this, we calculated the ΔE_S of **19** (29.6 kJ mol^{-1}) in BuCN, which provides a predicted $T_{1/2}$ of 274 K. This is in excellent agreement with the experimentally determined approximate $T_{1/2}$ of 261(7) K using variable temperature UV-vis measurements (Fig. S27 and 28†), illustrating the predictive ability of this method for different solvents.

3.4.2 Case 2: effect of a single solvent on various complexes. We proceeded to analyze how a specific solvent influences the $T_{1/2}$ of various complexes (*i.e.*, why the $T_{1/2}$ value in MeCN is observed to be greater for **15** than **19**). Despite having similar ΔE_S, the overall shift in $T_{1/2}$ towards higher temperatures for the set of solvents for **15** compared to **19**, originates from the underlying difference in relative electronic energy for **15** ($\Delta E_{Gas} = -8.9$ kJ mol^{-1}) compared to **19** ($\Delta E_{Gas} = -17.2$ kJ mol^{-1}). This indicates that the $T_{1/2}$ of various complexes in a specific solvent is impacted by both ΔE_S and ΔE_{Gas}. Therefore, we correlated the $T_{1/2}$ values with the sum of the calculated ΔE_S and ΔE_{Gas} values for complexes **6**, **15** and **19** in MeCN and DCM (Table 7 and Fig. 8). We also extended this approach to the family of neutral [Co(3,5-dbdiox)(3,5-dbsq)(N_2L)] complexes (Chart S1 and Table S22†) with their experimentally measured $T_{1/2}$ values in toluene (Fig. 8).

The correlation derived between the ΔE_S + ΔE_{Gas} parameter and experimental $T_{1/2}$ can also act as a tool for determining the $T_{1/2}$ of a complex in a specific solvent. Calculating the ΔE_S + ΔE_{Gas} values for complex **47^0** in DCM (29.0 kJ mol^{-1}) and MeCN (30.1 kJ mol^{-1}) results in predicted $T_{1/2}$ values of 334 and 396 K respectively. The roughly estimated experimental switching points of **47^0** in DCM and MeCN were found to be ~313 and ~345 K, illustrating the possibility of determining $T_{1/2}$ values for various complexes.[93] With this, we demonstrate that the suggested approach and the parameter ΔE_S is broadly applicable across both families of Co–dioxolene complexes. Solvent/s or complexes that show a deviation from this general trend likely do so due to encompassing specific solute–solvent interactions.

Considering the solvent polarity argument has been commonly hypothesised as having an influence on VT equilibria, we sought to explore whether the change in dipole moment accompanying the VT interconversions is related to the solvent stabilisation energy. The dipole moment (μ) was calculated to be larger for the LS-Co^{III}-cat tautomer than HS-Co^{II}-sq state (ESI Section 12: Energy and dipole moment, Table S23†), resulting in a negative dipole change upon thermally-induced VT ($\Delta\mu = \mu_{HS\text{-}CoII\text{-}sq} - \mu_{LS\text{-}CoIII\text{-}cat}$). The calculated dipole moments for both tautomers are larger when including MeCN compared to the gas phase (Table S23†), demonstrating the impact of the dielectric medium around the molecule causing a stabilisation in electronic energies (Tables S23 and S24†). The complexes with similar ΔE_S values had similar changes in the change in dipole moment ($\Delta\mu$) (Tables 6, S23 and S25†). Plotting the ΔE_S (MeCN) *versus* $\Delta\mu$ of various complexes shown in Table 6 results in a linear correlation (Fig. 9) with $R^2 = 0.89$. The correlation indicates that the larger the change in dipole moment upon valence tautomeric transition, the greater the solvent stabilisation energy. Therefore, the sensitivity of the VT interconversion to the nature of the solvent correlates with the difference in dipole between the two tautomers.

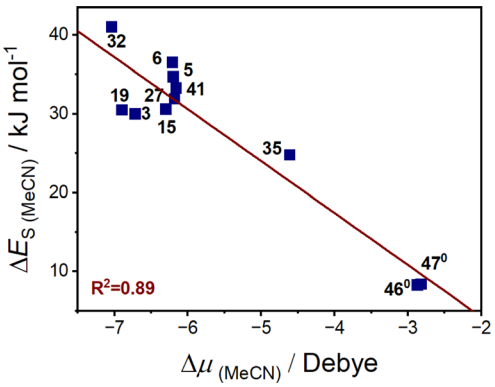

Fig. 9 Correlation of calculated ΔE_S in MeCN with change in dipole moment of the complex (calculated with M06L-D4/def2-TZVPP, in MeCN).

While exceptions are possible due to specific solvent–solute interactions that have not been accounted for in this study, this analysis provides a rationale for the observations regarding the behaviour of VT complexes in different solvents. The dipole argument also explains why the lower polarity DCM and DCE, with solvent polarity index (PI) of 3.1 and 3.5 respectively, compared to acetone (PI = 5.1) and MeCN (PI = 5.8) more effectively stabilise the HS-Co^{II}-sq tautomer, which has a smaller dipole moment. From this DFT analysis, we have shown that the variation in transition temperature with solvent arises from the effect of solvent stabilisation energy. The magnitude of this effect correlates with the change in dipole moment for a given complex during VT and is notably less for the neutral [Co(diox)(sq)(N_2L)] *versus* the cationic [Co(diox)(N_4-L)]$^+$ families, with the VT for the neutral complexes therefore much less sensitive to environment. Indeed the neutral complexes **46^0** and **47^0**, which are least susceptible to environmental effects, have been successfully doped into polystyrene films with retention of VT functionality.[114] In contrast, the high degree of change in dipole moment imparted for [Co(dioxophen)(cth)]$^+$ (**32**) is consistent with its observed propensity for macroscopic polarisation driven VT interconversion.[115]

4 Conclusions

We have utilised literature monocationic [Co(diox)(N_4L)]$^+$ complexes, in conjunction with previous DFT studies on neutral [Co(diox)(sq)(N_2L)] complexes, to benchmark a wide selection of DFT methods with solvent, relativistic, thermal and dispersion effects. This has allowed identification of M06L-D4/def2-TZVPP as a robust, reliable, and computationally inexpensive level of

theory for the analysis of VT in both main families of Co–dioxolene VT complexes. Application of this chosen method to over thirty literature $[Co(diox)(N_4L)]^+$ complexes accurately captured the experimental behaviour of the Co–dioxolene complexes with over 97% accuracy. We also confirmed the predictive power of the computational model by synthesising and characterising three new complexes, two of which exhibit thermally-induced VT in both the solid-state and in solution, while the third remains in the LS-Co^{III}-cat form across all temperatures, in agreement with prediction.

The development of this accurate DFT-based strategy allowed us to analyze the molecular origin of VT for the two major classes of neutral and monocationic Co–dioxolene complexes and elucidate the experimentally observed dependence on solvent. Deconvolution and quantification of various effects contributing to the VT equilibrium demonstrated that solvent stabilisation plays a dominant role, varying significantly from ~8 kJ mol^{-1} for neutral complexes to ~33 kJ mol^{-1} for cationic complexes. This variation was found to originate from the magnitude of dipole moment change during VT interconversion; the larger the dipole change, the greater the effect of the solvent. This explains why solvents with a lower polarity index stabilise the HS-Co^{II}-sq state. Two major factors govern the position of VT equilibrium: (1) the underlying intrinsic tautomeric energy seperation (ΔE_{Gas}), and (2) the solvent stabilisation energy (ΔE_S). The experimentally determined $T_{1/2}$ values correlate with the combined $\Delta E_S + \Delta E_{Gas}$ effect. This correlation is consistent with experimental observations for numerous complexes in a number of solvents and provides a clear answer to the long-standing question of how solvent affects VT equilibria.

The dependence of the VT interconversion on the immediate environment of the Co–dioxolene species reflects the magnitude of the change of dipole moment accompanying the interconversion, which is larger for the charged complexes than the neutral. This understanding can potentially guide the selection and design of complexes tailored for incorporation into media that impart different molecular environments including thin films and polymers. Specifically, the neutral complexes with smaller change in dipole moment are likely best suited to retain VT properties upon incorporation into a polymer film. In contrast, a cationic complex with a larger change in dipole moment may display greater sensitivity for deployment in solvent/vapor sensing.

In summary, our quantitative and computationally inexpensive DFT-based strategy requires only a simple gas phase calculation to pre-screen hypothetical Co–dioxolene molecules to accurately predict if a molecule will exhibit thermally-induced VT. The solvent-dependent $T_{1/2}$ values and solvent-sensitivity can also be predicted. Straightforward calculation of the change of dipole moment that accompanies the VT interconversion indicates the sensitivity to environment and can inform the deployment of VT complexes in soft materials for future applications.

Finally, electron transfer and solvent-dependence have an importance in chemistry far beyond VT in Co–dioxolene systems. Solvent also influences VT in complexes with other redox-active metals and ligand. Solution SCO is affected by solvent, with this attributed in some cases to solvent polarity, although a comprehensive analysis is lacking. Solvent is also important for electron transfer in mixed-valence metal complexes, affecting intervalence charge transfer bands, with analyses suggesting the dielectric continuum plays a role.[116] In synthetic chemistry, transition metal photocatalysts typically utilises long-lived triplet excited states to conduct a wide range of chemical reactions. The effect of solvent on the excited state, and therefore catalytic function, has been an area of research and debate. The insights provide from this work into the influence on solvent-sensitivity of the change in dipole moment between different electronic states of a metal complex has broad relevance. So too, does the demonstration that properly benchmarked, reliable DFT approaches are powerful for understanding these critical chemical relationships.

Data availability

Crystallographic data for all compounds have been deposited with the CCDC under deposition numbers 2287379–2287395 and can be obtained from **https://www.ccdc.cam.ac.uk/**. Other data are available from the authors upon reasonable request.

Author contributions

FZMZ performed computational and experimental investigations. MAH assisted with synthesis. FZMZ, MAH and JTJ collected crystallographic data. RWG assisted with crystallographic structure solution and refinement LG provided computational supervision and project support. CB helped conceptualise the project and provided funding and supervision. FZMZ wrote the manuscript with contributions from all authors.

Conflicts of interest

There are no conflicts to declare.

Acknowledgements

CB thanks the Australian Research Council for funding (DP220100398 and LE210100009). LG is thankful for the allocation of computing resources by the National Computational Infrastructure (NCI) National Facility within the National Computational Merit Allocation Scheme (project no. fk5) and The University of Melbourne's Research Computing Services and the Petascale Campus Initiative (project no. punim0094). This research was additionally supported by the Research Computing Services NCI Access scheme at The University of Melbourne. FZMZ acknowledges Tina Tezgarevska and Vincent Nadurata for valuable discussions and Dr Marcus Giansiracusa and Dr Alex Duan for technical and instrumental assistance. This research was undertaken in part using the MX1 and MX2 beamlines at the Australian Synchrotron, part of ANSTO, Victoria, Australia, and made use of the ACRF detector. This work was also performed in part at the Trace Analysis for

Chemical, Earth and Environmental Sciences (TrACEES) Platform at the University of Melbourne.

References

1 M. R. Wasielewski, M. D. E. Forbes, N. L. Frank, K. Kowalski, G. D. Scholes, J. Yuen-Zhou, M. A. Baldo, D. E. Freedman, R. H. Goldsmith, T. Goodson, M. L. Kirk, J. K. McCusker, J. P. Ogilvie, D. A. Shultz, S. Stoll and K. B. Whaley, *Nat. Rev. Chem*, 2020, **4**, 490–504.
2 S. L. Bayliss, D. W. Laorenza, P. J. Mintun, B. D. Kovos, D. E. Freedman and D. D. Awschalom, *Science*, 2020, **370**, 1309–1312.
3 E. Coronado, *Nat. Rev. Mater.*, 2020, **5**, 87–104.
4 A. Dei and D. Gatteschi, *Angew. Chem., Int. Ed.*, 2011, **50**, 11852–11858.
5 N. Xin, J. Guan, C. Zhou, X. Chen, C. Gu, Y. Li, M. A. Ratner, A. Nitzan, J. F. Stoddart and X. Guo, *Nat. Rev. Phys.*, 2019, **1**, 211–230.
6 M. M. Paquette, D. Plaul, A. Kurimoto, B. O. Patrick and N. L. Frank, *J. Am. Chem. Soc.*, 2018, **140**, 14990–15000.
7 S. Fortier, J. J. Le Roy, C. H. Chen, V. Vieru, M. Murugesu, L. F. Chibotaru, D. J. Mindiola and K. G. Caulton, *J. Am. Chem. Soc.*, 2013, **135**, 14670–14678.
8 A. Dei, D. Gatteschi, C. Sangregorio and L. Sorace, *Acc. Chem. Res.*, 2004, **37**, 827–835.
9 D. Antonangeli, J. Siebert, C. M. Aracne, D. L. Farber, A. Bosak, M. Hoesch, M. Krisch, F. J. Ryerson, G. Fiquet and J. Badro, *Science*, 2011, **331**, 64–67.
10 O. Kahn and C. J. Martinez, *Science*, 1998, **279**, 44–48.
11 S. Rat, M. Piedrahita-Bello, L. Salmon, G. Molnár, P. Demont and A. Bousseksou, *Adv. Mater.*, 2018, **30**, 1–6.
12 A. Enriquez-Cabrera, A. Rapakousiou, M. Piedrahita Bello, G. Molnár, L. Salmon and A. Bousseksou, *Coord. Chem. Rev.*, 2020, **419**, 213396.
13 F. Novio, E. Evangelio, N. Vazquez-Mera, P. González-Monje, E. Bellido, S. Mendes, N. Kehagias and D. Ruiz-Molina, *Sci. Rep.*, 2013, **3**, 1–7.
14 K. S. Murray, in *Spin-Crossover Materials: Properties and Applications*, John Wiley & Sons Ltd, New York, 2013.
15 S. K. Karuppannan, A. Martín-Rodríguez, E. Ruiz, P. Harding, D. J. Harding, X. Yu, A. Tadich, B. Cowie, D. Qi and C. A. Nijhuis, *Chem. Sci.*, 2021, **12**, 2381–2388.
16 E. Resines-Urien, M. Á. G. García-Tuñón, M. García-Hernández, J. A. Rodríguez-Velamazán, A. Espinosa and J. S. Costa, *Adv. Sci.*, 2022, **9**, 1–7.
17 J. Villalva, A. Develioglu, N. Montenegro-Pohlhammer, R. Sánchez-de-Armas, A. Gamonal, E. Rial, M. García-Hernández, L. Ruiz-Gonzalez, J. S. Costa, C. J. Calzado, E. M. Pérez and E. Burzurí, *Nat. Commun.*, 2021, **12**, 1–8.
18 I. A. Gural'skiy, C. M. Quintero, J. S. Costa, P. Demont, G. Molnár, L. Salmon, H. J. Shepherd and A. Bousseksou, *J. Mater. Chem. C*, 2014, **2**, 2949–2955.
19 L. J. Kershaw Cook, R. Kulmaczewski, R. Mohammed, S. Dudley, S. A. Barrett, M. A. Little, R. J. Deeth and M. A. Halcrow, *Angew. Chem., Int. Ed.*, 2016, **55**, 4327–4331.
20 H. Phan, J. J. Hrudka, D. Igimbayeva, L. M. Lawson Daku and M. Shatruk, *J. Am. Chem. Soc.*, 2017, **139**, 6437–6447.
21 S. Rodríguez-Jiménez, M. Yang, I. Stewart, A. L. Garden and S. Brooker, *J. Am. Chem. Soc.*, 2017, **139**, 18392–18396.
22 R. M. Buchanan and C. G. Pierpont, *J. Am. Chem. Soc.*, 1980, **102**, 4951–4957.
23 G. K. Gransbury and C. Boskovic, in *Encyclopedia of Inorganic and Bioinorganic Chemistry*, Wiley, 2021, pp. 1–24.
24 T. Tezgerevska, K. G. Alley and C. Boskovic, *Coord. Chem. Rev.*, 2014, **268**, 23–40.
25 G. K. Gransbury, B. N. Livesay, J. T. Janetzki, M. A. Hay, R. W. Gable, M. P. Shores, A. Starikova and C. Boskovic, *J. Am. Chem. Soc.*, 2020, **142**, 10692–10704.
26 P. Wang, G. P. A. Yap and C. G. Riordan, *Inorg. Chim. Acta*, 2019, **488**, 49–55.
27 D. Kovala-Demertzi, S. K. Hadjikakou, M. A. Demertzis and Y. Deligiannakis, *J. Inorg. Biochem.*, 1998, **69**, 223–229.
28 P. Leeladee, R. A. Baglia, K. A. Prokop, R. Latifi, S. P. de Visser and D. P. Goldberg, *J. Am. Chem. Soc.*, 2012, **134**, 10397–10400.
29 M. P. Van Koeverden, B. F. Abrahams, D. M. D'Alessandro, P. W. Doheny, C. Hua, T. A. Hudson, G. N. L. Jameson, K. S. Murray, W. Phonsri, R. Robson and A. L. Sutton, *Chem. Mater.*, 2020, **32**, 7551–7563.
30 A. Aumüller, P. Erk, G. Klebe, S. Hünig, J. U. von Schütz and H.-P. Werner, *Angew. Chem., Int. Ed.*, 1986, **25**, 740–741.
31 A. K. Pal, C. Li, G. S. Hanan and E. Zysman-Colman, *Angew. Chem., Int. Ed.*, 2018, **57**, 8027–8031.
32 K. G. Alley, G. Poneti, P. S. D. Robinson, A. Nafady, B. Moubaraki, J. B. Aitken, S. C. Drew, C. Ritchie, B. F. Abrahams, R. K. Hocking, K. S. Murray, A. M. Bond, H. H. Harris, L. Sorace and C. Boskovic, *J. Am. Chem. Soc.*, 2013, **135**, 8304–8323.
33 G. K. Gransbury, M. E. Boulon, S. Petrie, R. W. Gable, R. J. Mulder, L. Sorace, R. Stranger and C. Boskovic, *Inorg. Chem.*, 2019, **58**, 4230–4243.
34 K. G. Alley, G. Poneti, J. B. Aitken, R. K. Hocking, B. Moubaraki, K. S. Murray, B. F. Abrahams, H. H. Harris, L. Sorace and C. Boskovic, *Inorg. Chem.*, 2012, **51**, 3944–3946.
35 D. M. Adams, A. Dei, A. L. Rheingold and D. N. Hendrickson, *J. Am. Chem. Soc.*, 1993, **115**, 8221–8229.
36 Y. Mulyana, G. Poneti, B. Moubaraki, K. S. Murray, B. F. Abrahams, L. Sorace and C. Boskovic, *Dalton Trans.*, 2010, **39**, 4757–4767.
37 A. Bencini, A. Caneschi, C. Carbonera, A. Dei, D. Gatteschi, R. Righini, C. Sangregorio, J. Van Slageren and J. Van Slageren, *J. Mol. Struct.*, 2003, **656**, 141–154.
38 V. L. Nadurata and C. Boskovic, *Inorg. Chem. Front.*, 2021, **8**, 1840–1864.
39 C. Reichardt, *Chem. Rev.*, 1994, **94**, 2319–2358.
40 D. M. Adams, B. Li, J. D. Simon and D. N. Hendrickson, *Angew. Chem., Int. Ed.*, 1995, **34**, 1481–1483.
41 G. D'Avino, L. Grisanti, J. Guasch, I. Ratera, J. Veciana and A. Painelli, *J. Am. Chem. Soc.*, 2008, **130**, 12064–12072.

42 J. T. Janetzki, F. Z. M. Zahir, R. W. Gable, W. Phonsri, K. S. Murray, L. Goerigk and C. Boskovic, *Inorg. Chem.*, 2021, **60**, 14475–14487.
43 P. Hohenberg and W. Kohn, *Phys. Rev.*, 1964, **136**, B864–B871.
44 W. Kohn and L. J. Sham, *Phys. Rev.*, 1965, **140**, A1133–A1138.
45 M. Bursch, J. Mewes, A. Hansen and S. Grimme, *Angew. Chem.*, 2022, **134**, e202205735.
46 L. Goerigk and N. Mehta, *Aust. J. Chem.*, 2019, **72**, 563–573.
47 S. Grimme, S. Ehrlich and L. Goerigk, *J. Comput. Chem.*, 2011, **32**, 1456–1465.
48 S. Grimme, J. Antony, S. Ehrlich and H. Krieg, *J. Chem. Phys.*, 2010, **132**, 15410.
49 S. Grimme, A. Hansen, J. G. Brandenburg and C. Bannwarth, *Chem. Rev.*, 2016, **116**, 5105–5154.
50 L. Goerigk and S. Grimme, *J. Chem. Theory Comput.*, 2010, **6**, 107–126.
51 F. Neese, *Coord. Chem. Rev.*, 2009, **253**, 526–563.
52 V. I. Minkin, A. G. Starikov and A. A. Starikova, *Pure Appl. Chem.*, 2018, **90**, 811–824.
53 G. K. Gransbury, M.-E. Boulon, R. A. Mole, R. W. Gable, B. Moubaraki, K. S. Murray, L. Sorace, A. Soncini and C. Boskovic, *Chem. Sci.*, 2019, **10**, 8855–8871.
54 Y. Zhao and D. G. Truhlar, *J. Chem. Phys.*, 2006, **125**, 194101.
55 E. Caldeweyher, S. Ehlert, A. Hansen, H. Neugebauer, S. Spicher, C. Bannwarth and S. Grimme, *J. Chem. Phys.*, 2019, **150**, 154122.
56 F. Weigend and R. Ahlrichs, *Phys. Chem. Chem. Phys.*, 2005, **7**, 3297–3305.
57 F. Neese, *Wiley Interdiscip. Rev.: Comput. Mol. Sci.*, 2012, **2**, 73–78.
58 F. Neese, *Wiley Interdiscip. Rev.: Comput. Mol. Sci.*, 2018, **8**, 4–9.
59 F. Neese, F. Wennmohs, U. Becker and C. Riplinger, *J. Chem. Phys.*, 2020, **152**, 224108.
60 J. P. Perdew, *Phys. Rev. B: Condens. Matter Mater. Phys.*, 1986, **33**, 8822–8824.
61 J. P. Perdew, *Phys. Rev. B: Condens. Matter Mater. Phys.*, 1986, **34**, 7406.
62 A. D. Becke, *Phys. Rev. A*, 1988, **38**, 3098–3100.
63 S. Grimme, J. G. Brandenburg, C. Bannwarth and A. Hansen, *J. Chem. Phys.*, 2015, **143**, 054107.
64 S. Miertuš, E. Scrocco and J. Tomasi, *Chem. Phys.*, 1981, **55**, 117–129.
65 M. Cossi, N. Rega, G. Scalmani and V. Barone, *J. Comput. Chem.*, 2003, **24**, 669–681.
66 E. Van Lenthe, E. J. Baerends and J. G. Snijders, *J. Chem. Phys.*, 1993, **99**, 4597–4610.
67 O. A. Vydrov and T. Van Voorhis, *J. Chem. Phys.*, 2010, **133**, 244103.
68 E. Caldeweyher, C. Bannwarth and S. Grimme, *J. Chem. Phys.*, 2017, **147**, 034112.
69 T. Tezgerevska, E. Rousset, R. W. Gable, G. N. L. L. Jameson, E. C. Sañudo, A. Starikova and C. Boskovic, *Dalton Trans.*, 2019, **48**, 11674–11689.
70 J. P. Perdew, K. Burke and M. Ernzerhof, *Phys. Rev. Lett.*, 1996, **77**, 3865–3868.
71 N. C. Handy and A. J. Cohen, *Mol. Phys.*, 2001, **99**, 403–412.
72 L. Goerigk and S. Grimme, *Phys. Chem. Chem. Phys.*, 2011, **13**, 6670–6688.
73 N. Mardirossian and M. Head-Gordon, *J. Chem. Phys.*, 2015, **142**, 074111.
74 J. G. Brandenburg, C. Bannwarth, A. Hansen and S. Grimme, *J. Chem. Phys.*, 2018, **148**, 06410.
75 A. Najibi and L. Goerigk, *J. Chem. Theory Comput.*, 2018, **14**, 5725–5738.
76 A. D. Becke, *J. Chem. Phys.*, 1993, **98**, 5648–5652.
77 P. J. Stephen, F. J. Devlin, C. F. Chabalowski and M. J. Frisch, *J. Phys. Chem.*, 1994, **98**, 11623–11627.
78 V. N. Staroverov, G. E. Scuseria, J. Tao and J. P. Perdew, *J. Chem. Phys.*, 2003, **119**, 12129–12137.
79 N. Mardirossian and M. Head-Gordon, *Phys. Chem. Chem. Phys.*, 2014, **16**, 9904–9924.
80 N. Mardirossian and M. Head-Gordon, *J. Chem. Phys.*, 2016, **144**, 214110.
81 S. Grimme, *J. Chem. Phys.*, 2006, **124**, 034108.
82 L. Goerigk and S. Grimme, *J. Chem. Theory Comput.*, 2011, **7**, 291–309.
83 C. Metzger, R. Dolai, S. Reh, H. Kelm, M. Schmitz, B. Oelkers, M. Sawall, K. Neymeyr and H. Krüger, *Chem.–Eur. J.*, 2023, **29**, 0–3.
84 A. Singh, S. Panda, S. Dey and G. K. Lahiri, *Angew. Chem., Int. Ed.*, 2021, **60**, 11206–11210.
85 A. Beni, A. Dei, S. Laschi, M. Rizzitano and L. Sorace, *Chem.–Eur. J.*, 2008, **14**, 1804–1813.
86 A. Dei, A. Feis, G. Poneti and L. Sorace, *Inorg. Chim. Acta*, 2008, **361**, 3842–3846.
87 T. Mibu, Y. Suenaga, T. Okubo, M. Maekawa and T. Kuroda-Sowa, *Inorg. Chem. Commun.*, 2020, **114**, 107826.
88 A. Panja, *RSC Adv.*, 2013, **3**, 4954.
89 O. Sato, A. Cui, R. Matsuda, J. Tao and S. Hayami, *Acc. Chem. Res.*, 2007, **40**, 361–369.
90 A. A. Starikova, M. G. Chegerev, A. G. Starikov and V. I. Minkin, *Comput. Theor. Chem.*, 2018, **1124**, 15–22.
91 A. Dei and L. Sorace, *Appl. Magn. Reson.*, 2010, **38**, 139–153.
92 M. Radoń, *Phys. Chem. Chem. Phys.*, 2019, **21**, 4854–4870.
93 E. Evangelio, C. Rodriguez-Blanco, Y. Coppel, D. N. Hendrickson, J. P. Sutter, J. Campo and D. Ruiz-Molina, *Solid State Sci.*, 2009, **11**, 793–800.
94 F. Yu and B. Li, *Inorg. Chim. Acta*, 2012, **392**, 199–203.
95 A. F. M. da Silva, M. V. P. de Mello, J. G. Gómez, G. B. Ferreira and M. Lanznaster, *Eur. J. Inorg. Chem.*, 2019, **2019**, 1784–1791.
96 K. Katayama, M. Hirotsu, I. Kinoshita and Y. Teki, *Dalton Trans.*, 2014, **43**, 13384–13391.
97 M. G. Chegerev, D. V. Korchagin, G. V. Shilov, N. N. Efimov, A. G. Starikov, A. V. Piskunov, A. V. Chernyshev, A. N. Bulgakov, V. I. Minkin, A. V. Palii and S. M. Aldoshin, *Dalton Trans.*, 2022, **51**, 16876–16889.
98 T. Mibu, A. Iba, Y. Suenaga, T. Okubo, M. Maekawa, T. Kuroda-Sowa and K. Sugimoto, *Inorg. Chim. Acta*, 2021, **527**, 120538.

99 M. Graf, G. Wolmershäuser, H. Keim, S. Demeschko, F. Meyer and H. J. Krüger, *Angew. Chem., Int. Ed.*, 2010, **49**, 950–953.
100 A. Panja and A. Frontera, *Eur. J. Inorg. Chem.*, 2018, **2018**, 924–931.
101 A. Moledo Vicente Guedes, L. Sodré de Abreu, I. A. V. Maldonado, W. S. Fernandes, T. M. Cardozo, R. A. Allão Cassaro, M. Scarpellini and G. Poneti, *RSC Adv.*, 2023, **13**, 20050–20057.
102 R. C. Batista, F. da Silva Miranda, C. B. Pinheiro and M. Lanznaster, *Eur. J. Inorg. Chem.*, 2018, **2018**, 612–616.
103 Y. H. Guo, Y. M. Zhang, A. H. Li and F. Yu, *Acta Crystallogr. E*, 2011, **67**, 8380–8390.
104 S. Alvarez, D. Avnir, M. Llunell and M. Pinsky, *New J. Chem.*, 2002, **26**, 996–1009.
105 S. Llunell, M. Casanova, D. Cirera, J. Alemany and P. Alvarez, *SHAPE, version 2.1*, 2013.
106 R. Ketkaew, Y. Tantirungrotechai, P. Harding, G. Chastanet, P. Guionneau, M. Marchivie and D. J. J. Harding, *Dalton Trans.*, 2021, **50**, 1086–1096.
107 S. N. Brown, *Inorg. Chem.*, 2012, **51**, 1251–1260.
108 C. Piguet, *J. Chem. Educ.*, 1997, **74**, 815–816.
109 D. F. Evans, *J. Chem. Soc.*, 1959, 2003–2005.
110 A. Dei, G. Poneti and L. Sorace, *Inorg. Chem.*, 2010, **49**, 3271–3277.
111 I. Ratera, C. Sporer, D. Ruiz-Molina, N. Ventosa, J. Baggerman, A. M. Brouwer, C. Rovira and J. Veciana, *J. Am. Chem. Soc.*, 2007, **129**, 6117–6129.
112 V. L. Nadurata, M. A. Hay, J. T. Janetzki, G. K. Gransbury and C. Boskovic, *Dalton Trans.*, 2021, **50**, 16631–16646.
113 G. Cioncoloni, H. M. Senn, S. Sproules, C. Wilson and M. D. Symes, *Dalton Trans.*, 2016, **45**, 15575–15585.
114 D. M. Adams and D. N. Hendrickson, *J. Am. Chem. Soc.*, 1996, **118**, 11515–11528.
115 S. Q. Wu, M. Liu, K. Gao, S. Kanegawa, Y. Horie, G. Aoyama, H. Okajima, A. Sakamoto, M. L. Baker, M. S. Huzan, P. Bencok, T. Abe, Y. Shiota, K. Yoshizawa, W. Xu, H. Z. Kou and O. Sato, *Nat. Commun.*, 2020, **11**, 5–10.
116 D. M. D'Alessandro and F. R. Keene, *Chem. Soc. Rev.*, 2006, **35**, 424–440.